Università degli Studi di Padova

DIPARTIMENTO DI FISICA E ASTRONOMIA "GALILEO GALILEI"
Corso di Laurea Magistrale in Astronomia

Tesi di laurea magistrale

Old stellar populations in the bulge of the Milky Way

Revising TRILEGAL calibration in view of a new VVV catalogue based on PSF photometry

Laureando:
Alessandro Mazzi
Matricola 1149595

Relatore:
Prof.ssa Paola Marigo

Co-relatori:
Dr. Léo Girardi
Dr. Piero Dal Tio

Anno Accademico 2017-2018

SOMMARIO

Molti autori hanno studiato la struttura e la popolazione stellare della Via Lattea per comprendere la sua formazione e la sua evoluzione. Tali studi però hanno spesso fatto affidamento su un solo tipo di tracciante stellare o hanno utilizzato survey poco profonde o ancora hanno impiegato modelli non omogenei o non aggiornati. Anche se i loro risultati sono stati utili per comprendere alcune delle caratteristiche del bulge, ad oggi ancora manca una visione coerente costruita su solide basi.

Il modello di sintesi di popolazione TRILEGAL è capace di simulare la fotometria di qualsiasi campo nella Via Lattea tenendo conto della storia di formazione stellare, della relazione età-metallicità, della funzione di massa iniziale, delle diverse componenti della Galassia e del sistema fotometrico. Vista Variables in the Via Lactea (VVV) è una survey fotometrica di alta qualità che copre più di 300 gradi quadrati sul Centro Galattico, inclusa la regione del bulge ed i suoi dintorni. In questo lavoro è emersa una discrepanza tra le funzioni di luminosità simulata e osservata della finestra di Baade, la cui causa non è stata ancora identificata, ma potrebbe essere legata al miglioramento dei modelli che stanno alla base di TRILEGAL.

Allo scopo di riprodurre correttamente la funzione di luminosità delle stelle nella regione del bulge, è stata effettuata una revisione preliminare di due parametri chiave del modello: la densità centrale del bulge ρ_{bulge} e la distanza del Sole dal Centro Galattico $R_{\odot}$. La calibrazione usata in precedenza prevedeva $\rho_{\text{bulge}} = 406.0$ $\text{M}_{\odot}/\text{pc}^3$ e $R_{\odot} = 8700.0$ pc.

All'inizio è stata analizzata nel dettaglio solo la finestra di Baade. Sono stati simulati 18 modelli con diverse combinazioni dei parametri variando ρ_{bulge} del $\pm 10\%$ del valore originario e riducendo $R_{\odot}$ a passi del 5% dal valore iniziale fino a -25%. Per ciascun modello è stato calcolato il valore del χ^2 della funzione di luminosità simulata rispetto a quella osservata ed è poi stata costruita una griglia di χ^2. Quest'ultima ha evidenziato l'esistenza di una regione nella quale erano posizionati i modelli che riproducevano meglio le osservazioni. Per identificare con precisione il miglior modello, è stato utilizzato un algoritmo Levenberg-Marquardt, ma il risultato non è stato soddisfacente. La funzione di luminosità simulata infatti ancora non riproduceva quella osservata.

Per superare questo problema sono state considerate alcune modifiche.

L'intervallo in magnitudine della funzione di luminosità è stato ridotto a $K_s \in [12, 16]$ mag per evitare le stelle brillanti sature e per impedire che gli errori fotometrici nella coda a bassa luminosità influenzassero troppo la procedura. Una correzione del punto zero, benché piccola, è stata aggiunta a VVV per passare dal sistema fotometrico di VISTA a quello standard Vegamag, usato da TRILEGAL. È stato inoltre considerato un equivalente Poissoniano del χ^2. Infine, è stato introdotto un taglio in colore sia sul diagramma colore magnitudine osservato che su quello simulato per rimuovere quanto possibile le stelle del disco e concentrarsi su quelle del bulge.

Queste procedure hanno permesso di determinare un nuovo set di parametri che però, quando usato per simulare altri nove campi, ha prodotto risultati non omogenei. Alcuni campi erano riprodotti correttamente mentre altri avrebbero richiesto un set di parametri differente. In realtà, era eccessivo pretendere che solo da Baade Window, calibrando solamente due parametri, si potesse ottenere una riproduzione accurata di tutta la regione del bulge.

Applicando la procedura di ricerca del best fit ad ogni campo individualmente ha effettivamente mostrato che i parametri così derivati erano sparsi in un intervallo di densità del bulge e di distanze Sole-Centro Galattico, rendendo difficile la scelta del modello migliore. Una soluzione ideale sarebbe stata determinare il best fit contemporaneamente per tutti i campi, ma questo processo sarebbe stato molto più soggetto a cadere in minimi locali.

La scelta migliore è quindi stata quella di esplorare lo spazio dei parametri dei campi calcolando una griglia di χ^2 per ciascuno e successivamente sommare tutte le griglie insieme per determinare l'esistenza di un minimo. La griglia era composta da 80 punti con $\rho_{\text{bulge}} \in [300, 750]$ $M_\odot/\text{pc}^3$ a passo di 50 $M_\odot/\text{pc}^3$ e $R_\odot \in [7000, 8750]$ pc spaziati di 250 pc. Questa strategia ha mostrato che il minimo globale certamente esisteva ed era posizionato a $(\rho_{\text{bulge}}, R_\odot) = (400$ $M_\odot/\text{pc}^3$, 7750 pc). Questi valori saranno usati come punto di partenza della successiva, più accurata ricalibrazione del modello.

A causa dei metodi usati nella determinazione del miglior modello, la stima dell'incertezza totale sui parametri era complessa. Al contrario, gli errori statistici sono stati facilmente determinati. È stato lanciato un gran numero di simulazioni (100) del miglior modello e per ciascuna è stato calcolato il χ^2. La risultante distribuzione di χ^2 è quindi stata usata per definire una regione a 3σ degli errori statistici nello spazio dei parametri.

ABSTRACT

Various authors studied the structure and stellar population of the Milky Way bulge to investigate its formation and evolution. These studies however often relied on a single kind of target or employed shallow surveys or used non-homogeneous or non-updated models. Even if their results were useful to understand some of the characteristics of the bulge, a coherent picture constructed using a solid foundation is still missing.

The population synthesis model TRILEGAL can simulate the photometry of any field in the Milky Way accounting for the star formation history, the age-metallicity relation, the initial mass function, the different components of the Galaxy and the photometric system. The Vista Variables in the Via Lactea (VVV) is a high-quality infrared photometric survey that covers more than 300 squared degrees on the Galactic Centre, including the bulge region and its neighbourhood. In this work I highlight a mismatch between the simulated and observed luminosity function of Baade Window, whose cause has not yet been identified but may be related to the refinement of the models at the base of TRILEGAL.

This work presents a preliminary revision of the parameters used in the model to properly reproduce the luminosity distribution of the stars on the bulge region. In particular, I determined new values for the bulge central density ρ_{bulge} and for the Sun-Galactic Centre distance $R_\odot$.

Initially, only Baade Window was subject to a detailed analysis. Computing a sparse grid of χ^2 for different combinations of parameters pointed to the existence of a region where the solution was likely located. A Levenberg-Marquardt algorithm was then implemented to pinpoint with higher accuracy the values of the parameters at the solution, but the result was not completely satisfactory. In fact the simulated luminosity function still did not closely reproduce the observed one.

To overcome this issue a number of adjustments were considered. The magnitude range of the luminosity function was restricted to $K_{\mathrm{s}} \in [12, 16]$ mag to avoid the bright saturated stars and to prevent the large photometric errors found in the faint tail from influencing too much the fit. A zero point correction, though fairly small, was applied to VVV to bring it from the VISTA photometric system to the standard Vegamag one used by TRILEGAL. Also, a Poisson

equivalent of the χ^2 was implemented. Finally, a colour cut was introduced on both the observed and the simulated colour magnitude diagram to remove most of the disk stars and concentrate on fitting the bulge ones.

These procedures allowed to determine a new set of parameters that however, when used to simulate nine other fields, produced non-homogeneous fits. Some fields were reproduced correctly while others would have required a different set of parameters. Indeed, it was unreasonable to expect that from Baade Window alone, adjusting only two parameters, a perfect fit for the whole bulge region could have been achieved.

Fitting each field individually indeed showed that the derived parameters were spread in a range of bulge densities and Sun-GC distances, making it difficult to determine the best model. An ideal solution would have been to fit at the same time all the fields, but this process would have been more susceptible to falling into local minima.

The best choice was then to explore the parameters space of the fields computing a grid of χ^2 for each one and later summing them all together to check for the existence of a minimum. The grid consisted of 80 grid points for $\rho_{\text{bulge}} \in [300, 750] \text{ M}_\odot/\text{pc}^3$ with a step of 50 $\text{M}_\odot/\text{pc}^3$ and $R_\odot \in [7000, 8750]$ pc with a spacing of 250 pc. This approach showed that the global minimum definitely existed and was located around $(\rho_{\text{bulge}}, R_\odot)$=(400 $\text{M}_\odot/\text{pc}^3$, 7750 pc). These values will be used as the starting point for the subsequent more accurate recalibration of the model.

Due to the methods used in the determination of the best model, the estimate of the total uncertainty on these parameters was complicated. The statistical errors on the other hand could be easily estimated. A large number of simulations (100) of the best model were performed and from each one the χ^2 value was calculated. The resulting χ^2 distribution was then used to mark a 3σ region of statistical error in the parameters space.

ACKNOWLEDGMENTS

INDICE

1 | THE MILKY WAY

The Milky Way is a fundamental reference point to understand disk galaxies and an essential test for galactic formation and evolution models. However, given our position inside the Disk, studying its structure is difficult and understanding its formation and evolution is possibly harder. For this purpose, both high quality data and accurate models that account for any structure and substructure are needed. Thanks to the large wealth of data on the Milky Way accumulated during the years by several extensive surveys of our galaxy, a global picture of the Milky Way has emerged and three main components were identified and characterised: the Halo, the Disk and the Bulge. This chapter presents a brief overview of the structure of the Milky Way galaxy.

1.1 THE HALO

The Halo is the outermost component of the Milky Way. It can be divided in three separate components: the Stellar Halo, the Hot Halo and the Dark Halo.

The stellar component of the Halo constitutes about 1% of the total stellar mass. In the classical picture it is composed of old, metal-poor stars with large random motions that date back to the time of the formation of the galaxy (Eggen et al., 1962). Motivated by the presence of multiple components and substructures, it is assumed that it formed mainly through tidal disruption of satellites, according to the hierarchical formation model, during the early stages of the formation of the Galaxy about 10 Gyr ago. The inner part of the Stellar Halo is older than the outer one and may have been formed partly by stars ejected from the Disk and partly by stars originated from the gas stripped from the accreted satellites. The Stellar Halo is generally described as a flattened axisymmetric distribution with a double power-law radial profile and there is some evidence that the flattening parameter increases with galactocentric distance. There is also an evident steepening of the density profile with a break radius of $R_{s} = 25 \pm 10$ kpc, but the value of the outer slope depends on the halo tracer used in the study. Summing the estimates of the mass of the "smooth" Stellar Halo obtained from models to that of the substructures, a total mass of a few 10^{8} M$_{\odot}$ is derived (Bland-Hawthorn and Gerhard, 2016).
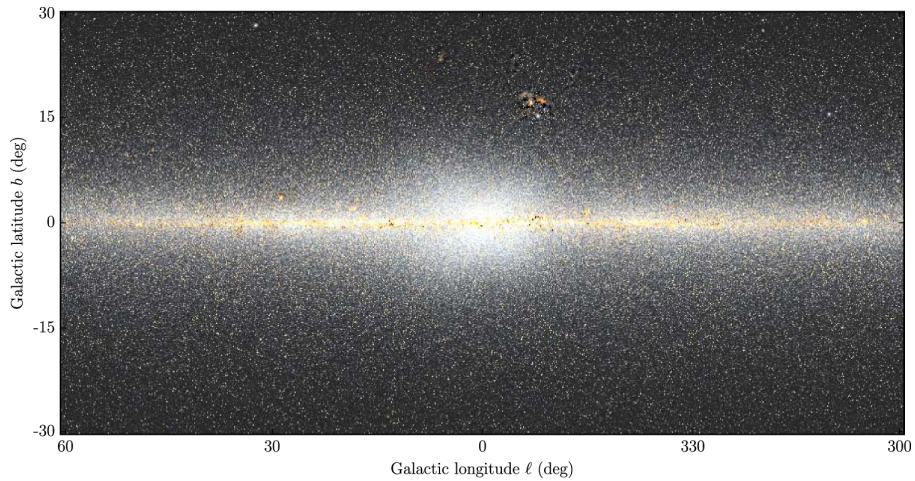
Figura 1: View of the Milky Way from the combination of the W1 and W2 bands of the WISE survey highlighting the boxy shape of the bulge and hinting at its X-shape. From Ness and Lang (2016).

The Hot Halo, made up of hot diffuse plasma, is detected in the X-rays as a background along any line of sight and as absorption of OVII and OVIII in the direction of AGNs and continues to interact with the environment through in-falls and outflows. The detailed results about the structure and the mass of this component are uncertain due to the sensitivity of X-rays surveys, the presence of the Local Bubble and the solar wind charge exchange processes. Despite these difficulties, it seems that the Hot Halo mass is approximately of the order of a few 10^{10} M$_\odot$ and it is likely composed of two parts with different structure and metallicity.

Finally, the Dark Halo is described as an oblate spheroid with a stronger flattening in the inner part and a quasi-spherical shape in the outer one, but there is no clear agreement on this issue. Its mass is not clearly determined, but combining results from the kinematics of halo stars and satellites, from the modelling of tidal streams and from the requirement on the "timing mass"[1] an estimate of the virial mass of roughly 1×10^{12} M$_\odot$ can be derived.

1.2 THE DISK

The disk of the Milky Way is a flat structure that defines the Galactic Plane and can be clearly seen in Figure 1 at very small galactic latitudes. The Solar system

---

[1] This means that the masses of the Galaxy and of M31 must be sufficiently large to produce the observed kinematics.
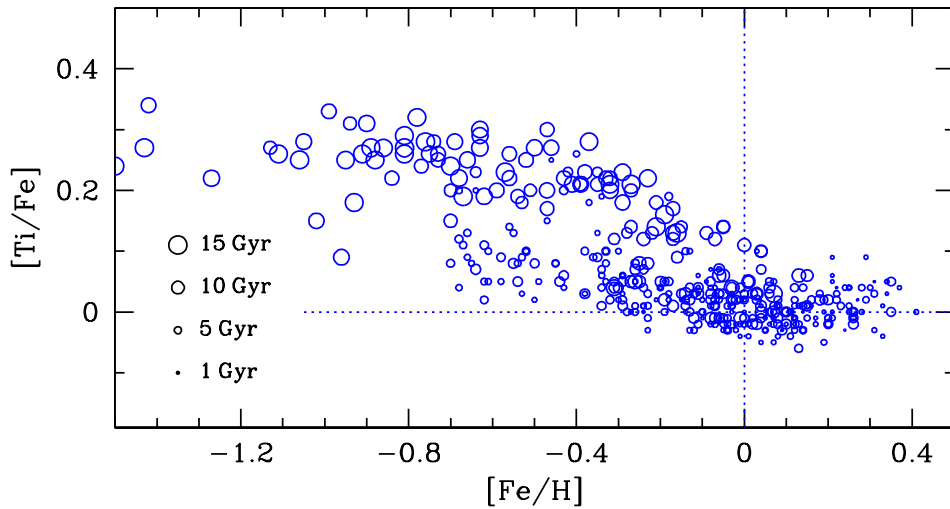
Figura 2: [Ti/Fe] versus [Fe/H] for a subset of the 700+ F and G dwarf stars analysed by Bensby et al. (2014) that had a low age uncertainty.

is placed inside it, at a small vertical distance from the Galactic Plane between the Carina-Sagittarius and Perseus arms.

Even if a completely self-consistent picture of the entire Disk has yet to emerge, the presence of two separate components called the thin disk and thick disk is confirmed. In fact, even though the thin one is dominant, the other one emerges as an older, more elevated and chemically distinguished structure (Bensby et al. (2014), Figure 2). It is today established that the thick disk also features a larger α enhancement compared to the thin disk. It is not yet clear if they have a distinct formation history and whether the thick disk may have been formed by the migration and/or flaring of the old disk stars (Bland-Hawthorn and Gerhard, 2016). An exponential function is generally used to fit the photometry of both but particular attention needs to be paid to the Disk's substructures, such as the Virgo overdensity.

The outer boundary of the Disk seems to be located between 10 kpc and 15 kpc, but this point is still debated. Certainly there are evidences for warping and flaring from the Galactic Plane towards large distances from the Galactic Centre. These effects must be accounted for during the search for the edge of the Disk.

1.3 THE BULGE

The Bulge is the innermost component of the Milky Way. It can be resolved in stars but its structure and the populations that comprise it are difficult to study due to the presence of lots of dust in the Galactic Disk. Even so, it is continuously under study and its properties are being slowly unveiled. In particular, the recent discoveries on the three dimensional structure of the bulge are challenging the various theories on its formation and evolution.

Figure 1 presents a recent image of the central regions of the Milky Way obtained by Ness and Lang (2016) using WISE data. It highlights the boxy/peanut shape of the Galaxy and it should be noted how the left edge appears bigger than the right one due to the effects of the bar inclination.

1.3.1 Formation theories.

The hierarchical formation scenario states that at early times the merger processes dominated and favoured the formation of spheroids and the growth of a stellar disk could then lead to the formation of the so called classical bulges. These structures show hot dynamics similarly to elliptical galaxies and are composed of old ($\sim$ 10 Gyr) stars often showing metallicity gradient (more metal rich in the centre).

Afterwards secular evolution processes become relevant and disk instabilities form a bar in the inner disk. The bars, due to vertical instabilities, might then thicken and produce the central out-of-plane components that are observed as boxy/peanut bulges. These structures should present cylindrical rotation, which means that the velocity does not decrease with the height above the Galactic Plane, and since the bar can destabilize the gas in the disk and bring it to inner regions, a slow, continuous star formation should be achieved, determining the presence of a younger component. These structures are referred to as pseudo-bulges, are dominated by rotation and feature metal-rich stars.

1.3.2 Bar and X–shape

The boxy structure of the bulge was discovered in the images of the DIRBE instrument on board the COBE satellite by Dwek et al. (1995). This finding prompted a strong research activity on the bulge using all of the available techniques: kinematics, superficial density of stars, micro-lensing and more. The strongest limit was represented by the large extinction towards the inner regions of the Milky Way and soon the IR photometry was employed to largely reduce this issue. Earlier studies were largely based on 2MASS photometry (eg.
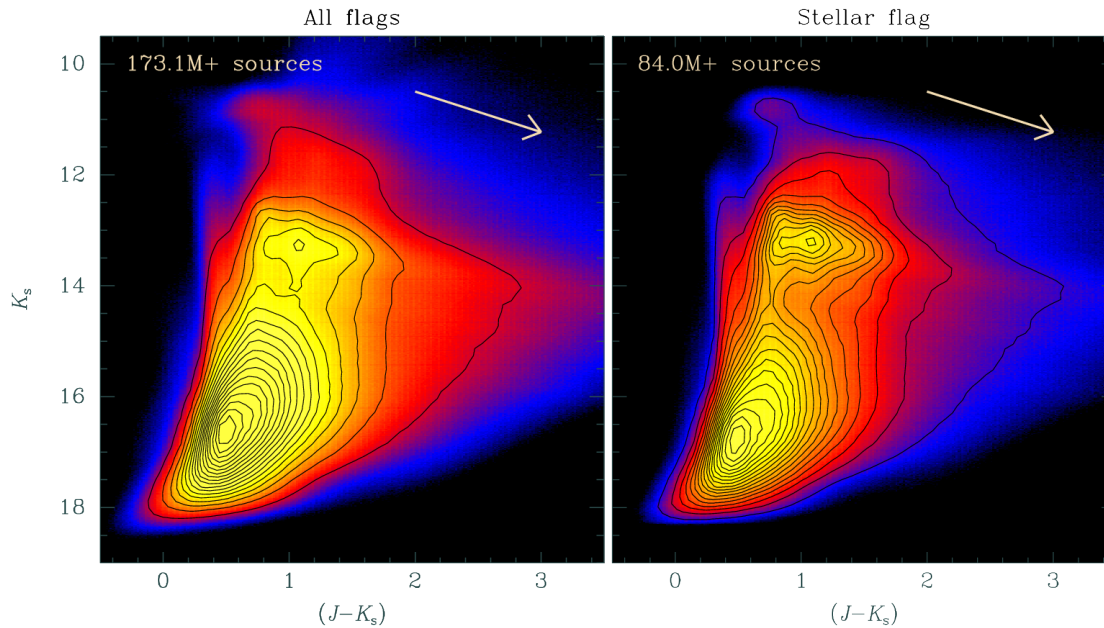
Figura 3: Left panel: colour-magnitude diagram obtained using all of the VVV sources. Right panel: colour-magnitude plot obtained using a selection of the VVV sources marked as "stellar". From Saito et al. (2012).

Vanhollebeke et al., 2009; see next section).

Saito et al. (2012) presented an analysis of the bulge based on its colour-magnitude diagram constructed from more than 84 million stellar sources detected by the VVV survey and illustrated in Figure 3. Even if this colour-magnitude diagram illustrated the complexity of the bulge, with populations at different ranges of magnitude and colour and affected differently by the extinction, with a hint of the X-shape of the bulge, an analysis on smaller regions was performed. This way not only the double peak of the RC appeared more clearly, but also its dependence on longitude and latitude was highlighted. In particular, the RC appeared to split at $|b| > 5°$ and the separation between the peaks grew larger at increasing galactic latitude up to $b = 8°$.

Wegg and Gerhard (2013) constructed a 3D model of the bar of the Milky Way using the VVV DR1 source catalogue due to its magnitude limit being four magnitudes deeper than the 2MASS one. They considered the RC stars, corrected their magnitude for extinction to determine a reliable line of sight density distribution and finally recovered the three dimensional density. From the modelling they determined that their 3D distribution was elongated and had an inclination angle with respect to the line of sight of $\alpha = (27 \pm 2)°$. More importantly, they noticed that for a height above the Galactic Plane larger

than about 400 pc the bulge appeared to have an X shape. Figures 4 and 5 present this fact: the former shows how the isophotes assume more and more an X-shape when moving away from the plane and the latter further illustrates how the density profile of the RC splits into two peaks at increasing z.

While the boxy/X-shaped structure of the bulge appears in images such as Figure 1, not all of the stars in the bulge are included in this structure. In fact Dékány et al. (2013) with OGLE and VVV data showed that the RR Lyrae stars, which represent an old and metal poor population ([Fe/H]~ -1), did not follow the distribution of the RC stars. In fact, they showed a spatial distribution centrally concentrated at about $R_0 = 8.33$ kpc and thus they did not trace the inclined bar. However, in the centre of this distribution a bar-like structure seemed to be present, probably due to momentum transfer between the bar and the initial classical bulge.

Finally, there are evidences of a smaller inner bar. While the main bar is estimated to be 2.5 kpc long and inclined of an angle between 15° and 30° with respect to the line of sight, Gonzalez et al. (2011) detected an anomalous position angle in the inner 1 kpc of the bulge for $-4° < l < 4°$. They proposed this as evidence of an inner bar characterised by a semi-major axis of about 500 pc and an inclination with respect to the line of sight of approximately 45°.

1.4 PREVIOUS ATTEMPTS AT MODELLING THE BULGE

Several authors tried to construct a complete and reliable model of the bulge relying on different kinds of data and aiming to explain most if not all of its features. Some of the most relevant efforts in this context are presented in the following.

Dwek et al. (1995) pioneered this field using the images from the DIRBE instrument on the COBE satellite at 1.25, 2.2, 3.5 and 4.9 μm to characterise the morphology of the bulge. They tested several models for the bulge: one oblate spheroid model; three Gaussian models; three exponential models; two power-law models. For all wavelengths the models that improved the fit the most were those with a flattening both along the vertical direction and the Galactic Plane, which meant "boxy" models. In particular, the best models were the Gaussian model G2 and the exponential model E3:

$$\rho_{G2}(x, y, z) = \rho_0 \exp(-0.5 r_s^2) \tag{1}$$
$$\rho_{E3}(x, y, z) = \rho_0 K_0(r_s) \tag{2}$$
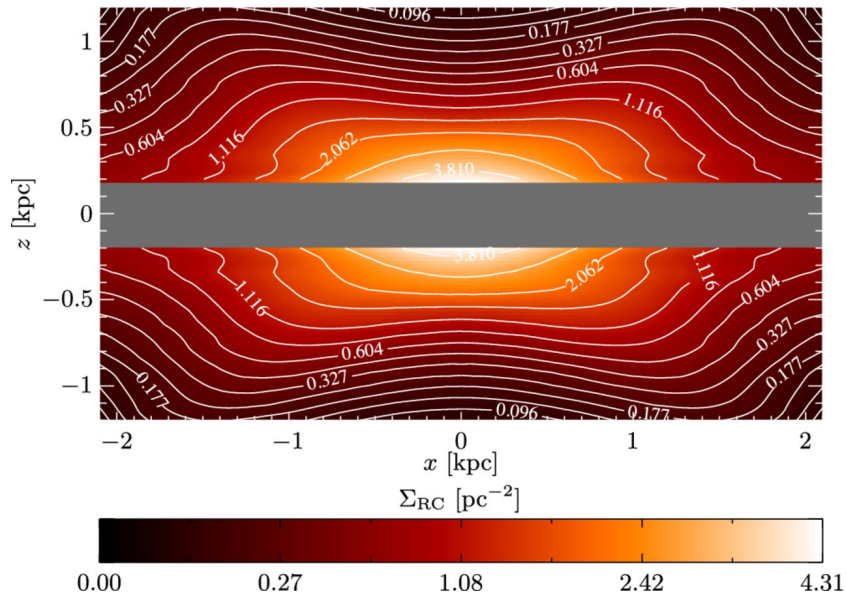
Figura 4: 3D density of the Milky Way bulge seen along the intermediate axis; the X-shape of the bulge naturally appears. From Wegg and Gerhard (2013).

Figura 5: Surface density of the RC stars for the view presented in Figure 4 over different slices above the Galactic Plane ($0.15 < z < 0.45$, red; $0.45 < z < 0.75$, green; $0.75 < z < 1.05$, blue; $1.05 < z < 1.2$, yellow; all units are kpc) highlighting the appearance of the X-shape structure while moving away from the Galactic Plane. From Wegg and Gerhard (2013).

where

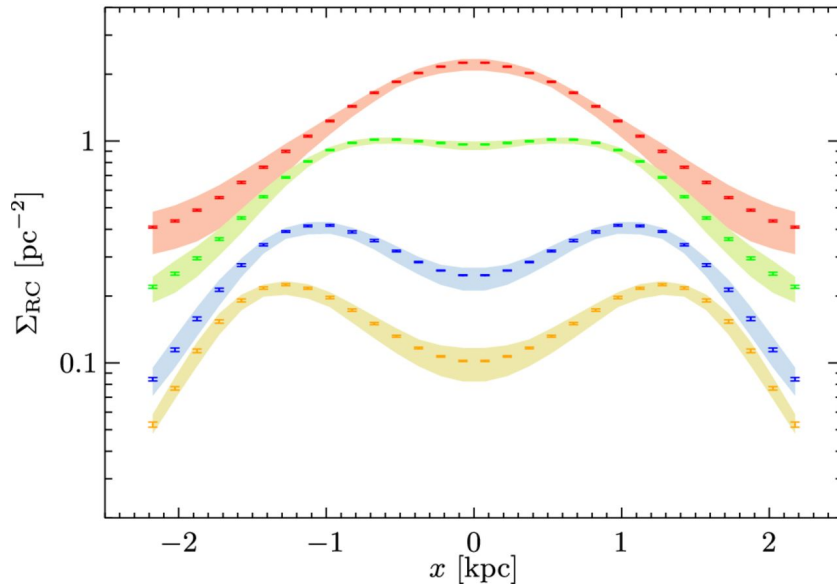$$r_s = \left\{ \left[\left(\frac{x}{x_0} \right)^2 \left(\frac{y}{y_0} \right)^2 \right]^2 + \left(\frac{z}{z_0} \right)^4 \right\}^{1/4} \tag{3}$$

and K_0 is a modified Bessel function. They highlighted that in the low latitude regions the intensity distribution was in general fitted better by an exponential function than by a Gaussian one. The model G3 was however an exception in that it resembled a Gaussian with a power law core (Bahcall distribution) described by

$$\rho_{G3} = \rho_0 r^{-1.8} \exp(-r^3) \tag{4}$$

and it could fit very well the innermost ($|b| \leq 0.5°$) regions of the bulge. With regards to the axis ratio, the best models predicted similar values and the average resulted $\{x_0, y_0, z_0\} = \{1 : 0.33 \pm 0.11 : 0.23 \pm 0.8\}$. The bulge triaxiality, defined as

$$\mathscr{T} = \frac{1 - (y_0/x_0)^2}{1 - (z_0/x_0)^2} \tag{5}$$

resulted in the range $0.81 - 0.94$, close to being a prolate spheroid. The rotation angle determined by their fitting was consistent with an inclination with respect to the line of sight spanning the interval $10° - 30°$, in line with previous works. No significant indication of a tilt with respect to the plane was detected.

The release of the uniformly-calibrated 2MASS data in the H (1.24 μm), J (1.66 μm) and K_s (2.16 μm) bands gave new momentum to the study of the bulge. Vanhollebeke et al. (2009) compared the output of the TRILEGAL galaxy model to these data, as well as the OGLE-II one, to retrieve the best model on several fields selected from the OGLE survey. They selected only the bulge stars in the colour-magnitude diagram and used the data in the K_s band to estimate the best parameters using a minimization procedure. Initially they obtained a distance to the Galactic Centre of $R_0 = 8.6$ kpc, an orientation angle with respect to the line of sight of $\phi = 20°$, a scale length of the bulge $a_m = 2.7$ kpc, a stellar density of $f_0 = 422.4$ M$_\odot$/pc^3 and axial ratios $1 : 0.69 : 0.30$. They tested different metallicity and age distribution and finally determined a best model with $R_0 = 8.7^{+0.57}_{-0.43}$ kpc, $\phi = 15°^{+12.7}_{-13.3}$, $a_m = 2.5^{+1.73}_{-0.16}$ kpc, $f_0 = 406.0^{+40.4}_{-167.3}$ M$_\odot$/pc^3 and $1 : 0.68^{+0.19}_{-0.05} : 0.31^{+0.04}_{-0.06}$.

Among the most important studies of the bulge, the one by Wegg and Gerhard (2013) outlined in the previous section is surely fundamental due to the identification of the X-shaped bulge. Several authors however proposed

alternative explanations to the presence of this feature. For example, some tried to disprove the existence of a true three dimensional X-shaped structure in the bulge originated as buckling of the bar in favour of an explanation based on the presence of chemically different stellar populations. Lee et al. (2015) based their remarks on the evidences of He enrichment of the bulge combined with observations of the globular cluster Terzan 5, which showed a double RC similar to that of the bulge. In addition, the bi-modality of the metallicity distribution function and the metallicity gradient found along the minor axis of the bulge suggested the presence of a composite bulge, made of a bar and a classical bulge. According to the authors, the latter showed the double RC feature due to the presence of a generation of stars G1 with standard He-enrichment, which populated the faint RC, and a generation G2 super He-rich populating bright RC, while the bar component was characterised by a single RC. With this theory they could explain the behaviour of the RC of the bulge. In fact, the double RC disappeared at low latitudes due to the masking by the bar and reappeared at larger latitudes from the Galactic Plane where the bar was weaker. Furthermore, the longitude effect was reproduced thanks to the superposition of the double RC of the classical bulge component, which is "fixed" at a certain distance, and the RC of the bar, whose position on the luminosity distribution changed as a result of the inclination of the bar. Figure 6 visually explains the longitude and latitude dependence of the double RC. Nevertheless, the authors also noted that a confirmation using star kinematics was necessary to asses the correctness of their results.

A similar reasoning based on the multiple population approach was applied by Lee and Jang (2016) to RR Lyrae stars from the OGLE survey. They showed that a single population model could not correctly describe the distribution of these stars, whereas a multiple population one with differences in the He content resulted much more appropriate. The latter evidence was in turn recognised by the authors as an argument in favour of the multiple population scenario as explanation of the double RC of the bulge.

López-Corredoira (2016) studied the stellar density of the bulge using F0-F5 main sequence stars, characteristic of the young (≤ 10 Gyr) bulge, whose distances were measured through photometric parallax. They considered sources from the VISTA-VVV survey in the J and H bands due to the low extinction values and considered the region with $|l| \leq 10°$ and $-10° \leq b \leq -6°$. Their results showed a single peaked density distribution with a distance of about 8 kpc which resulted larger at lower Galactic longitude due to the presence of the bar. Finally they compared their density with the one predicted by an X-shaped or boxy bulge model using the inclination of the bar derived by Wegg
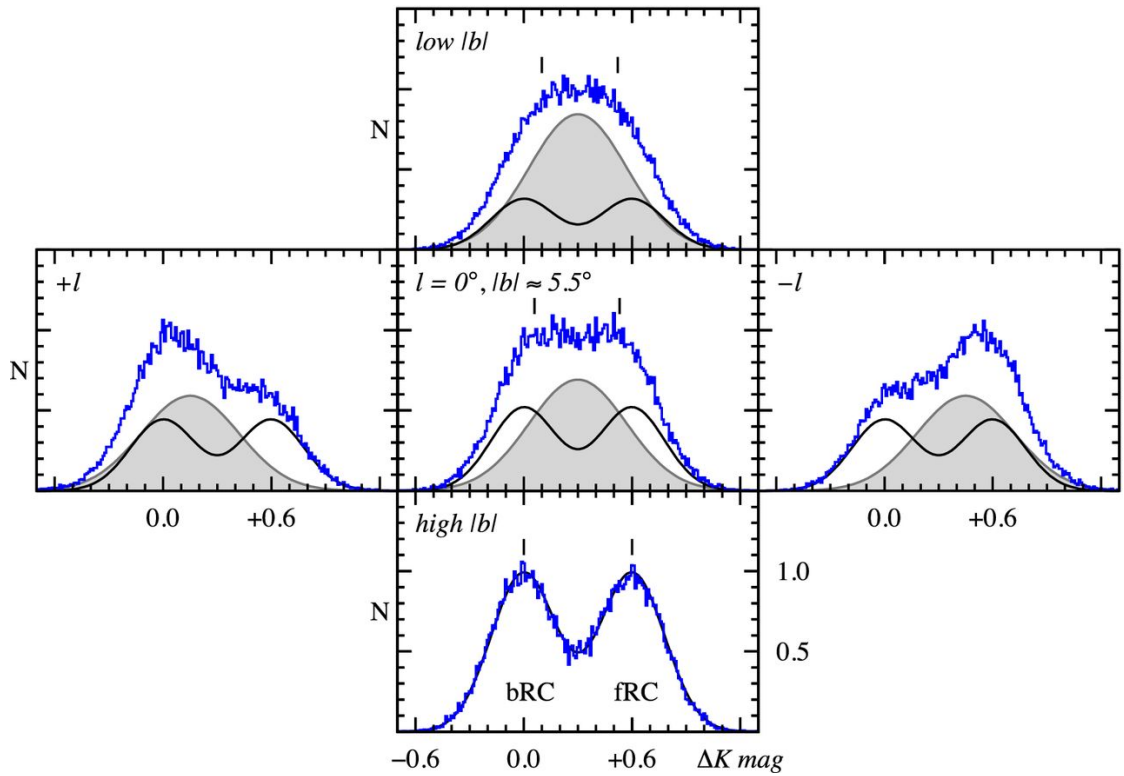
Figura 6: Latitude and longitude dependence of the RC shape (from simulations, blue histogram) resulting from the superposition of a classical bulge component with two stellar populations of different He-enrichment (in grey) and a bar component inclined of a certain angle with respect to the line of sight (black line). From Lee et al. (2015).

and Gerhard (2013), $\alpha = 27°$, and assuming a constant $R_0 = 8000$ pc, and claimed that the observations were consistent with a boxy rather than X-shaped bulge. However, for some lines of sight the predictions of the two models could not be properly distinguished. Another tracer is used by López-Corredoira (2017), namely Mira variable stars, with similar results and again challenging the acknowledgement of the X-shaped structure inside of the bulge.

1.5 MOTIVATION BEHIND THIS WORK

As illustrated above, many different works focused on modelling the shape of the bulge in order to understand its structure and its formation as well as its stellar population. However, most of them relied on a single kind of target (for example red clump stars) or employed data coming from shallow surveys of

the Milky Way (for example 2MASS) or used non-homogeneous models put together using data from multiple sources. Even if their works were extremely successful, it can be said that a global, coherent picture of the bulge constructed using a solid foundation is still missing.

The rationale behind this work, that nonetheless is intended as a preparatory step for a more extensive project, is to take advantage of the state-of-the-art surveys of the past few years to provide an uniform modelling of our Galaxy with a set of stellar tracks, isochrones, and population synthesis models as updated and self-consistent as possible.

2 | DATA

Choosing the right catalogue to be used as a reference for the simulations is a very significant step and may hinder the subsequent ones. In fact, specifically for the investigation of the bulge of the Galaxy, that catalogue should be able to grasp as much as possible the variety of details that comprise it. It should cover most, if not all, of its footprint on the sky, be deep enough to sample distances up to and beyond it, and be as much as possible complete. In addition, the problem of the presence of dust inside the Galactic Disk has to be taken into account. This requires observations either in the so called "windows" (line of sight directions along which the amount of dust is greatly reduced) or in photometric bands less affected by the extinction such as the IR ones.

Of the many surveys covering the bulge which are available to the public, the Vista Variables in the Via Lactea (VVV) survey (Minniti et al., 2010) better fits the requirements listed above.

2.1 VISTA VARIABLES IN THE MILKY WAY

The main purpose of this survey was to improve our knowledge of the Galaxy, including its formation, its structure and its stellar populations, combining the informations coming from photometry and variability studies of its inner regions. Using the near-IR camera VIRCAM of the 4m-class telescope VISTA, the Galactic Bulge and the inner Galactic Disk were observed in the Z, Y, J, H and K_s bands with a multi-epoch approach, covering approximately 520 squared degrees.

Compared to previous near-infrared surveys, VVV has a higher resolution, providing better photometry in very dense fields, and is deeper. The magnitude limit reached in most fields is generally $K_s \sim 18$ while in the most crowded regions it reaches $K_s \sim 16$. The 2MASS survey, for comparison, had a magnitude limit for unconfused sources at $|b| > 10°$ of 14.3 mag[1] in the K_s band.

---

[1] From https://www.ipac.caltech.edu/2mass/overview/about2mass.html

2.1.1 Telescope and camera

VISTA, short for Visible and Infrared Survey Telescope for Astronomy, has a 4.1 meter primary mirror, a 1.24 meter secondary and a focal ratio of f/3.25; the mirrors are coated with silver to optimize the IR performance and an active optics system composed of two low-order curvature sensors and a high order curvature one further enhances the quality of the observations.

The camera paired with this telescope is VIRCAM, VISTA InfraRed CAMera. It features 16 CCDs with 2048×2048 pixels each and a pixel scale of 0.34" arranged in a 4×4 array with large spacings. Two more sensors are used for guiding the telescope and another pair is used for active optics when the exposure time is longer than about 40 s. Unfortunately, a large area in the CCD number 16 is affected by bad pixels and must be accounted for. Figure 7 illustrates the arrangement of the CCDs.

It is necessary to point out that these detectors saturate at different levels, between 33000 and 35000 ADU, and in particular the CCD number five saturates at about 24000 ADU, the lowest of all. With regards to the problem of non-linearity of the detectors, it should be noted that the CCD number 13 has the highest non-linearity, but in any case this phenomenon occurs for any CCD approaching its saturation level. Even if corrections are applied during the data reduction phase, stars close to the saturation limit tend to deviate from their corresponding 2MASS magnitude.

A number of filters can be mounted on the camera[2]: the broad band Z (0.88 μm), Y (1.02 μm), J (1.25 μm), H (1.65 μm) and K_s (2.15 μm) as well as three narrow band filters centred on 0.98 μm, 0.99 μm and 1.18 μm. Figure 8 presents the transmission profile of these filters and the differences with several other surveys can be appreciated.

2.1.2 Observing strategy

The configuration of the 16 main detectors gave VIRCAM a field of view with a diameter of 1.65° but the area effectively covered by a single exposure was 0.599 deg², corresponding to a so called "pawprint". The first step to obtain the complete image of a field was taking two pawprints with a small offset to produce a "stacked pawprint". Afterwards, to fill the gaps between the detectors, the observations were repeated with fixed offsets to obtain six stacked pawprints. These images were then combined into a single "tile" whose area became approximately 1.501 deg². Figure 9 shows the Milky Way with superimposed the tiles that VVV acquired during its observations.

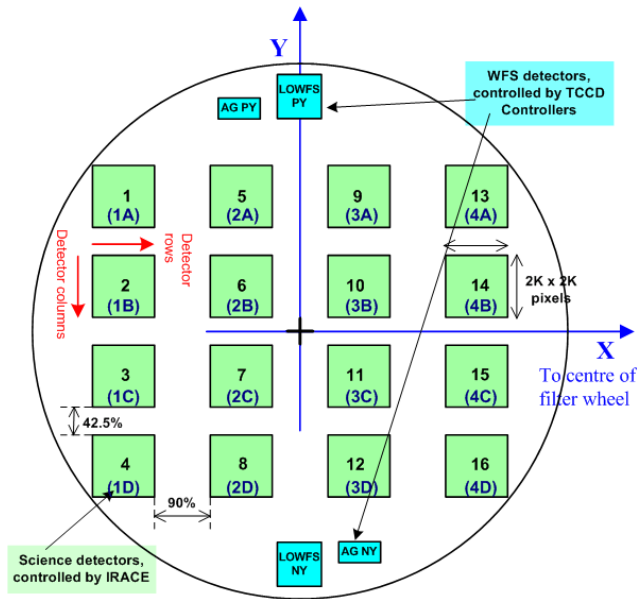[2] http://www.eso.org/sci/facilities/paranal/instruments/vircam/inst.html

Figura 7: Disposition of the 16 main detectors and the WFS at the focal plane of VIRCAM. From the VISTA instrumentation page[2] on the European Southern Observatory website.
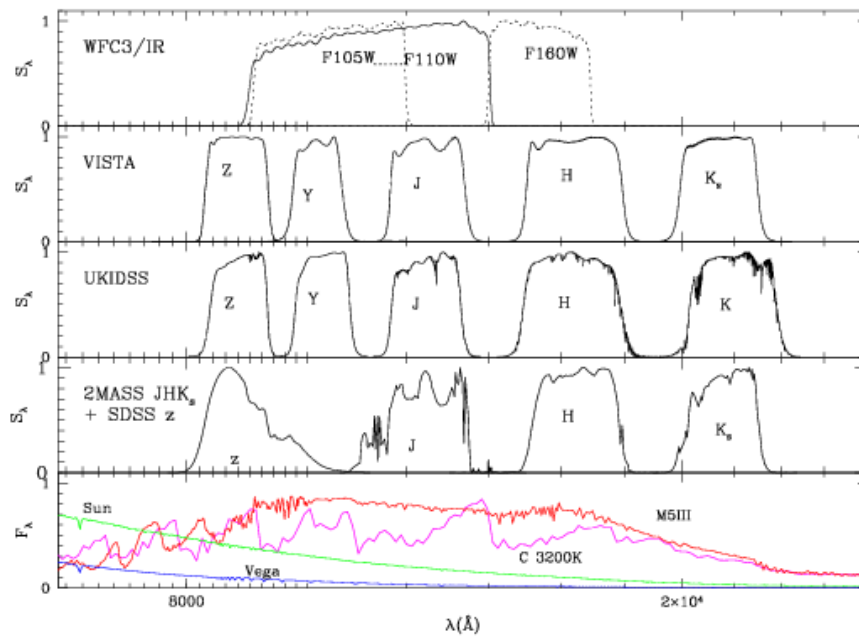

Figura 8: Transmission profiles of the filters used in different of surveys.
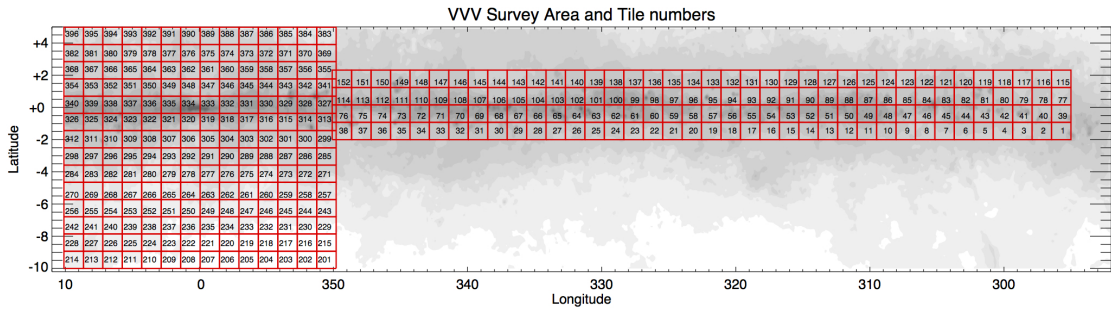
Figura 9: VVV surveyed area and tile numbering. From the VVV survey web page[3].

In total, 196 tiles were observed in the bulge and 152 in the southern disk for a total of 348 tiles for a total area of about 562 squared degrees. All of them were observed at least twice in the Z, Y, J and H filters, between 69 and 293 times in the K_s band for the bulge area, and between 48 and 52 times for the disk region.

2.1.3 VVV aperture catalogue and photometry

The images of the tiles underwent a series of correction steps before being ready to be used. Then, the position and fluxes in different apertures were computed and a kind of morphological classification was established, dividing the sources in classes such as "stellar object", "noise", "saturated" and more. The single band catalogues were matched together using astrometric corrections with a tolerance of one arcsecond to obtain a multi-band catalogue. Stars located in fields near the Galactic Plan, more affected by extinction, had a stronger requirement, consisting in the detection in the Z and Y bands.

The calibrations were determined using the 2MASS stars detected in the tiles. Starting from the instrumental magnitude m_{inst} in a given filter, to recover the calibrated ones m_{inst} the following equation (Saito et al., 2012) was used

$$m_{cal} = m_{inst} + ZP - k(X - 1) \tag{6}$$

where ZP is the zero-point, k is extinction coefficient and X is airmass.

Figure 10 presents the photometric errors in a typical disk field and in a crowded bulge one. The different extinction produces a noticeable effect, with the errors in the bulge region reaching significantly larger values at much brighter magnitudes with respect to the disk ones. Nonetheless, a small part of this behaviour is also due to the different exposure times.

---

[3] https://vvvsurvey.org/
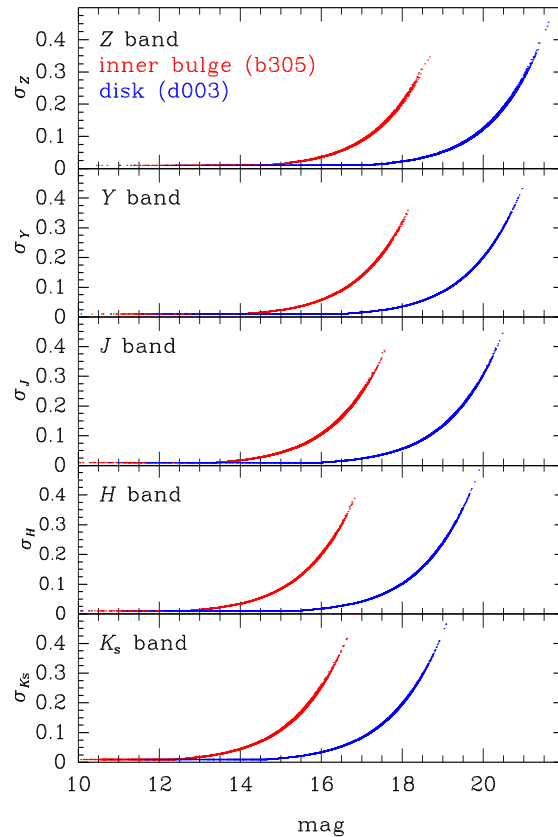
Figura 10: Comparison between the photometric errors in a disk field (d003) and one in the bulge (b305). The difference in mostly due to a different extinction, with a small contribution by the different exposure times. From Saito et al. (2012).

The completeness of the catalogue depends on the position in the bulge region. Using artificial star tests, Saito et al. (2012) analysed two bulge field with diametrically opposed crowding in the K_s band. They added 5000 stars at random positions with a PSF derived from isolated stars in the image. Figure 11 illustrates the result of this analysis and the different style of the lines stands for the method considered. The solid lines show the completeness estimated only through the fraction of recovered stars, that is artificial stars detected in positions within 1 px from the original one. The dashed lines highlight the consequence of adding a requirement on the recovered magnitude, specifically the latter needed to be within 0.5 mag from the original one. The second test in particular presents two important facts: the brightest stars tend to have a decreased completeness, most likely due to the saturation limit; the 50%
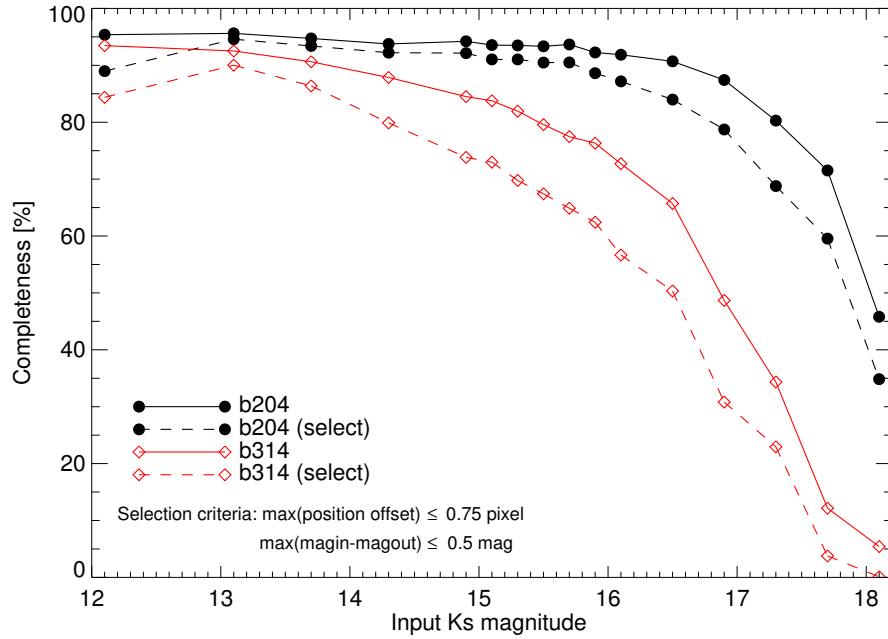
Figura 11: Result of the artificial star test in two bulge fields of different crowding. From Saito et al. (2012).

completeness is reached at $K_s \approx 18$ mag for the less crowded field while for the other this value is reached at $K_s \approx 16$ mag.

2.1.4 PSF photometry catalogue

The catalogue used in this study is not the one based on aperture photometry. In fact, when this technique is applied to the fields located near the Galactic Centre the resulting catalogue is affected by the very high crowding and the number of detected stars is much lower than it should be. The PSF photometry technique can overcome this obstacle and allow a larger number of stars to be identified.

The paper by Alonso-García et al. (2018) presents the construction of this catalogue. The stacked pawprints, less noisy than single pawprints and less troublesome to deal with than the tiles, were analysed with the DoPHOT software (Schechter et al. 1993; Alonso-García et al. 2012) to extract the sources. Each chip was studied separately with the aim to correct their individual issues (different saturation levels, bad pixels and such) and the borders observed only once were marked. The instrumental positions were converted into ecliptic coordinates and the instrumental magnitudes were calibrated using also a set of bright, non saturated sources to determine the zero points necessary to adopt

the VISTA photometric system. The six stacked pawprints were cross matched with 1 pixel tolerance and the magnitudes of the stars, if they were detected in more than one image, were computed as weighted averages with the errors from DoPHOT. This early catalogue was cross matched with a similar one obtained from the second epoch and only stars appearing in both, with the same tolerance as before, were kept. Eventually, all of the filters were cross matched and sources with a detection in at least three of them were added to the final catalogue.

The procedure outlined above has the merit of rejecting most of the spurious detections, but also has some weak points. First of all, variable sources are penalized: if their magnitude in the first and second epoch were too different it would cause their rejection from the catalogue. Also objects with velocities such that from the first epoch to the second they moved more than one pixel will be removed. It is nevertheless important to stress that the two epochs used to assemble the catalogue are characterised by different atmospheric and telescope conditions as well as the effect of the degradation of light sensitivity over time, which limits the chance to discover the dimmest objects in the later epochs. Moreover, some fields had only one epoch due to problems occurring in the other one.

The final PSF catalogue contains about 846 million sources, of which more 570 millions in the bulge region; a stellar density map for the latter region is illustrated in Figure 12.

The completeness was estimated by the authors with the artificial star experiment using 5000 stars. The results on the fields b208 (low crowding) and b319 (high crowding) are illustrated in Figure 13(a) and 13(b) respectively. Considering the K_s band, in low crowding fields the completeness is easily larger than 90% in the range of magnitudes between 12 mag and 17 mag, but in the most crowded ones it is larger than 80% only in the range from 12 mag to 14 mag and for larger magnitudes it quickly decreases, reaching 50% just past 16 mag.

2.1.5 Comparison between the catalogues

Alonso-García et al. (2018) made a comparison between the aperture catalogue based on VVV provided by CASU[4] and the afore mentioned PSF catalogue. The results on the same two fields mentioned above, b208 and b319, can be seen in Figure 14 where the number ratios of stars in the aperture and in the PSF catalogues are illustrated. Focusing on the K_s band, it is possible to appreciate

---

[4] http://casu.ast.cam.ac.uk/
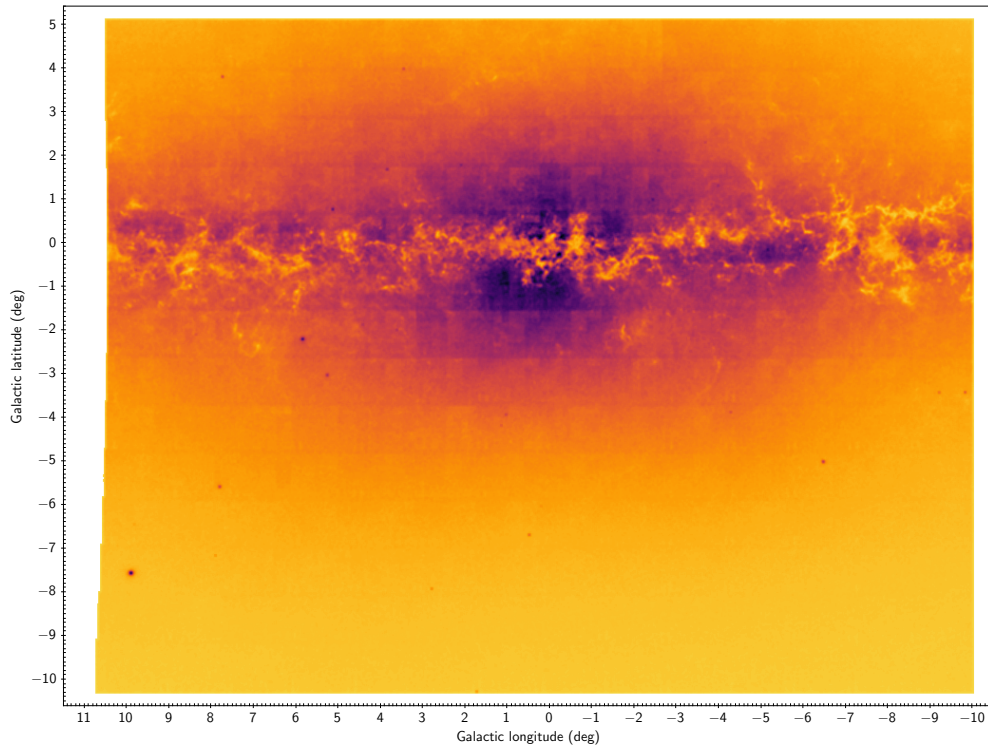
Figura 12: Density map of stars in the bulge area of VVV from the PSF catalogue. The density of the stars increases towards the Galactic Centre but on the Galactic Plane it decreases sharply due to the presence of dust. From Alonso-García et al. (2018).

that in the low crowding region (a) the PSF catalogue begins to give better results at magnitudes larger than about 13 mag, but in the high crowding one (b), except for the brightest magnitudes, the PSF catalogue clearly performed much better.

2.2 PIXELIZED CATALOGUE

The code used in this work, called TRILEGAL, can simulate a circular field of given area at the desired position in galactic longitude and latitude. Then, from the source catalogue, the stars that fall in a region centred on the same position and of equal area have to be extracted. This process is not always guaranteed to be easy and may require particular care.

To avoid any of the problems related to this aspect, the VVV PSF catalogue was pre-processed in the sense that it was divided in smaller regions according
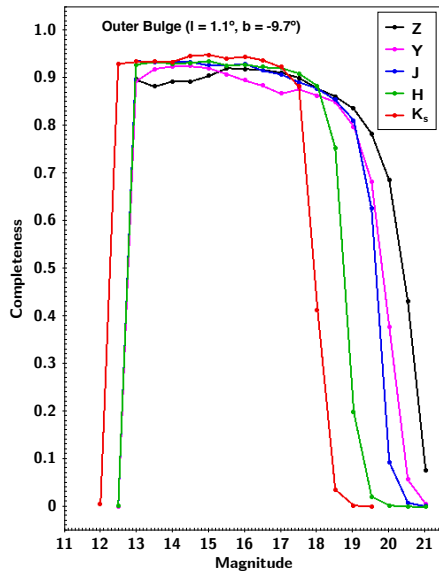
(a) Completeness for field b208.
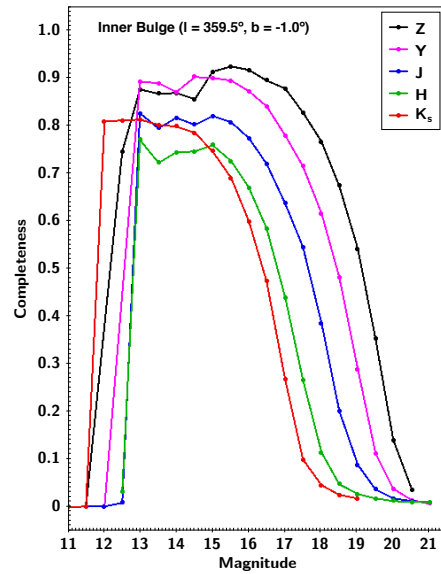
(b) Completeness for field b319.

Figura 13: Completeness computed with the artificial star experiment on two bulge fields. From Alonso-García et al. (2018).
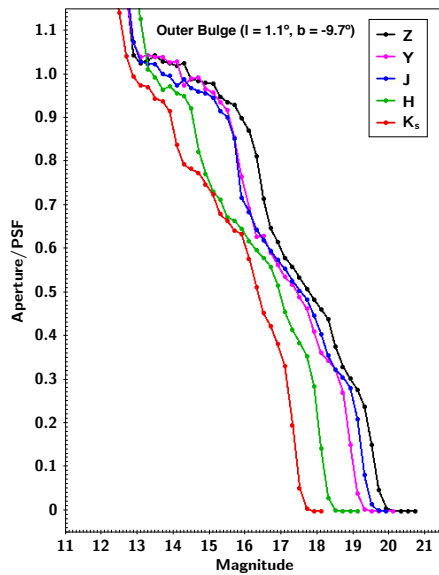
(a) Number ratio for field b208.

(b) Number ratio for field b319.

Figura 14: Ratio of the number of stars in the aperture catalogue and in the PSF one for a field with low crowding (a) and one with high crowding (b). From Alonso-García et al. (2018).
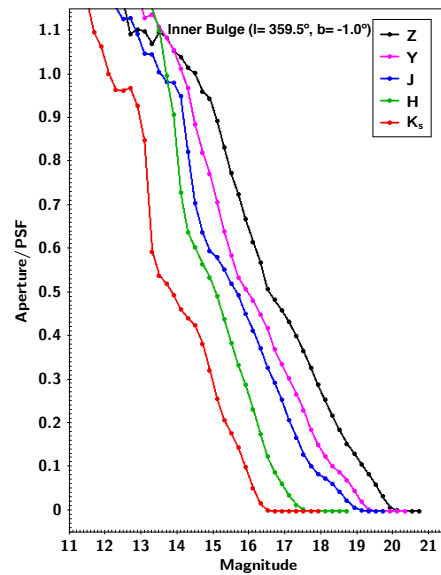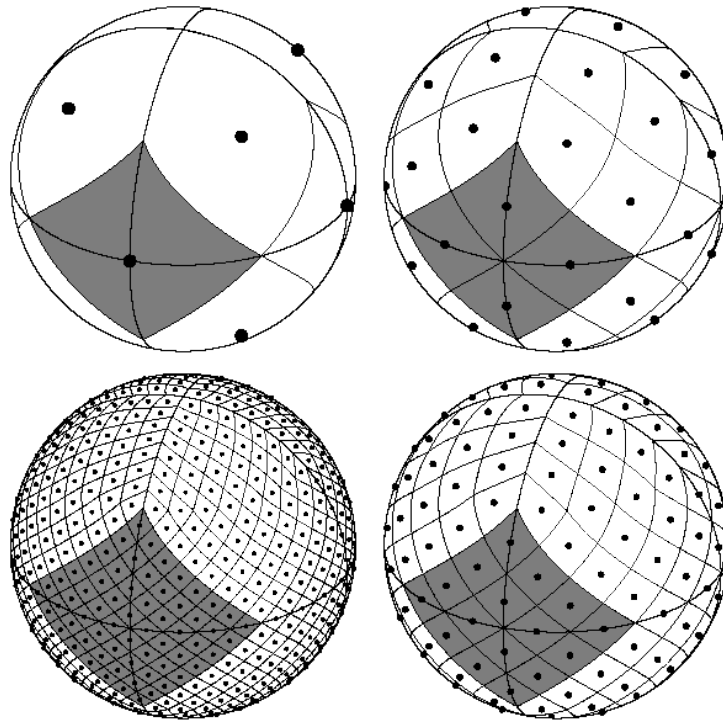
Figura 15: Subdivision of a sphere at different resolutions, specifically $N_{side} = 1, 2, 4, 8$. A base pixel is highlighted at all resolutions with a darker shade of colour. From the HEALPix web page.

to the Healpix scheme as discussed below.

2.2.1 Healpix

HEALPix (Górski et al. 2005; https://healpix.sourceforge.io) stands for Hierarchical Equal Area isoLatitude Pixelization of the sphere and provides and efficient method of dividing a spherical surface in subregions with equal area. The initial division consists of 12 pixels and this resolution is indicated by $N_{side} = 1$. In general, N_{side} represents the number of divisions along the side of a base pixel that are necessary to reach the desired resolution and it is necessarily a power of 2. The number of pixels at a given N_{side} can be easily computed as $N_{pix} = 12 \times N_{side}^2$. Figure 15 illustrates[5] the subdivision of a sphere at different resolutions, namely $N_{side} = 1, 2, 4, 8$.

All of the pixels are identified by three numbers: the value of their resolution, N_{side}, a power of two; an index p to distinguish them at a certain resolution,

---

[5] From https://healpix.sourceforge.io/.

N_{side}	area (deg^2)	N_{pix}
1	3438	12
256	0.05256	786432
2048	0.0008196	50331648

Tabella 1: Area and number of the pixels that correspond to the resolutions relevant for this work.

which varies between 0 and $12 \times N_{\text{side}}^2 - 1$; a unique index u that identifies exclusively the pixel with a specific N_{side} and p, computed as $u = p + 4 \times N_{\text{side}}^2$.

Regarding these indexes, HEALPix allows two different numbering schemes called "RING" and "NESTED". The first one causes the number of the pixels to increase along each iso-latitude ring from north to south. On the other hand the second numbering scheme arranges the pixels in tree structures.

2.2.2 Pixelization

The process of dividing the VVV PSF catalogue in pixels took advantage of the Python implementation of the HEALPix algorithm available through the module healpy[6]. In particular, the function ang2pix made it possible to determine which pixel, at the desired resolution, any star belonged to. The catalogue was created at a resolution of $N_{\text{side}} = 2048$ using the NESTED scheme and as a reference in Table 1 are listed the areas and the numbers of pixels for the base resolution ($N_{\text{side}} = 1$), for the resolution used for the simulations ($N_{\text{side}} = 256$), and for the one used in the catalogue ($N_{\text{side}} = 2048$).

Particular care had to be taken with the pixelization of the borders of the tiles. In fact, the bordering ones were actually overlapping and ignoring this detail would include twice the stars located in these overlapping regions. The method used to remove the duplicated stars was designed to be fast and simply rejected the stars from one of the two superimposing tiles. Even though it left some very small defects, these are not relevant for this work. A more accurate procedure will be implemented in the future.

---

[6] https://github.com/healpy/healpy

3 | MODELS

3.1 TRILEGAL

The TRIdimensional modeL of thE GALaxy (Girardi et al., 2005), TRILEGAL
hereafter, is a population synthesis model capable of simulating the stellar
photometry of any field in the Milky Way in any broad-band photometric
system given its central position and area. To achieve this goal it makes use
of a large number of libraries of evolutionary tracks and stellar spectra and
employs subroutines to perform the transformation of the models into different
photometric systems. It also takes into account the subdivision of the Galaxy
in its main components, namely the halo, the thin disk, the thick disk and the
bulge.

To simulate a field centred on a galactic coordinate (l, b) of angular size $d\Omega$
a Monte Carlo simulation is performed to generate the stars. Considering a
bin of width dm_λ, where λ stands for a passband, the number of stars with
magnitude in $[m_\lambda, m_\lambda + dm_\lambda]$ can be expressed as

$$N(m_\lambda, l, b) = dm_\lambda \int_0^\infty dr \, r^2 \, \rho(\bar{r}) \, \phi(M_\lambda, r) \, d\Omega \tag{7}$$

In the equation above $\rho(\bar{r})$ is the stellar density at $\bar{r} = (l, b, r)$ with r being line
of sight distance, M_λ is the absolute magnitude, linked to the apparent one m_λ
by

$$M_{0,\lambda} = m_\lambda - 5 \log(r) - A_\lambda(r) + 5 \tag{8}$$

where A_λ is the interstellar absorption in the band λ, and $\phi(M_\lambda, r)$ is the
intrinsic luminosity function. At this point it should be noted however that the
relative number of stars with different magnitudes and colours is constrained
by stellar evolution and population synthesis theories, thus providing a strict
condition to be satisfied by the model.

3.1.1 The description of the Galaxy in TRILEGAL

As already mentioned, the Milky Way can be divided into four main com-
ponents. In the model, each one is characterised by a set of parameters that

define their shape and density profile and by several files containing the star formation rate (SFR) and the age-metallicity relation (AMR). The initial mass function (IMF) used in this work is the one by Chabrier (2001). A more in-depth explanation of the model is given in Girardi et al. (2005).

HALO The halo can be described either through a $r^{-1/4}$ profile (de Vaucouleurs, 1959) or as an oblate spheroid; its parameters are the radial scale r_h, the oblateness b_h, and the local volume density of halo stars formed in the Solar System Ω_h.

THIN DISK The density distribution used for the thin disk is

$$\rho_\mathrm{d} = C_\mathrm{d} \exp\left(-\frac{R}{h_\mathrm{R}}\right) f(z) \tag{9}$$

where R is the galactocentric radius, h_R is the radial scale length and the constant C_d is determined in a way that reproduces a given total surface density of thin disc stars in the neighbourhood of the Sun, $\Sigma_\mathrm{d}(\odot)$. The function $f(z)$ represents the vertical distribution and is either an exponential or a squared hyperbolic secant function with a vertical scale height h_d. This scale is assumed to increase with time, meaning that stars are formed very close to the galactic plane with a scale height of z_0 and they move away as time passes:

$$h_\mathrm{d}(t) = z_0 \left(1 + \frac{t}{t_0}\right)^\alpha \tag{10}$$

THICK DISK The thick disk is described as a double exponential or an exponential times a squared hyperbolic secant function. Unlike the thin disk, the scale height is assumed to be independent of time since this component is mainly composed of populations older than 10 Gyr.

BULGE The number density of stars in the bulge follows the formalism of Binney et al. (1997) and is in line with the findings of Dwek et al. (1995). It is a truncated power law in the form

$$f_\mathrm{bulge} = f_0 \frac{e^{-a^2/a_\mathrm{m}^2}}{(1 + a/a_0)^{1.8}} \tag{11}$$

where a_m is the scale length, a_0 is the inner truncation length, f_0 is the stellar density and

$$a = \left(x^2 + \frac{y^2}{\eta^2} + \frac{z^2}{\xi^2} \right) \tag{12}$$

which describes a bulge with axis ratio $1 : \eta : \xi$. Other relevant parameters are the rotation with respect to the line of sight ϕ and the distance between the Sun and the Galactic Centre R_0. The two parameters studied in this work, namely the central density of the bulge and Sun-Galactic Centre distance, were set by Vanhollebeke et al. (2009) to $f_0 = 406.0 \, M_\odot/\text{pc}^3$ and $R_0 = 8.7$ kpc.

3.1.2 Dust/Extinction

The disk of the Milky Way is full of dust and accounting for its effects on light is crucial to obtain a good agreement with the observations. The standard implementation assumes that the dust is distributed on the Galactic Plane with an exponentially decreasing density in the orthogonal direction and a vertical scale height h_z^{dust}. The value of A_V is then evaluated on the line of sight using the dust density profile. To normalize the distribution the default method uses the value at infinity $A_{V,\infty}$ specified in the maps produced by the Planck mission (Planck Collaboration et al. (2014), Figure 16) but alternatively the local value of the absorption $A_{V,0}$ can be specified. From the value of extinction in the V band, the absorption in any other band is calculated simply by means of the A_λ/A_V ratios computed as in Girardi et al. (2002) and Girardi et al. (2008) for a Cardelli et al. (1989) extinction curve.

3.2 PHOTOMETRIC ERRORS

The model by itself does not take into account any form of error, in fact it produces a photometry which can be defined as "perfect". On the other hand, the catalogue of stars used as a reference is obviously affected by photometric errors. To deal with this aspect TRILEGAL accepts in input tables of photometric errors, one for each magnitude in the photometric system chosen for the simulation.

To provide a rough approximation of these errors, the ones listed in the VVV catalogue are used. For example, the distribution of the photometric errors of all the stars contained in the pixel of $N_{\text{side}} = 256$ located on Baade Window are illustrated in Figure 17. For each pixel, a mean value in magnitude bins of width 0.1 mag is computed and stored in a table which is used by TRILEGAL to simulate the errors.
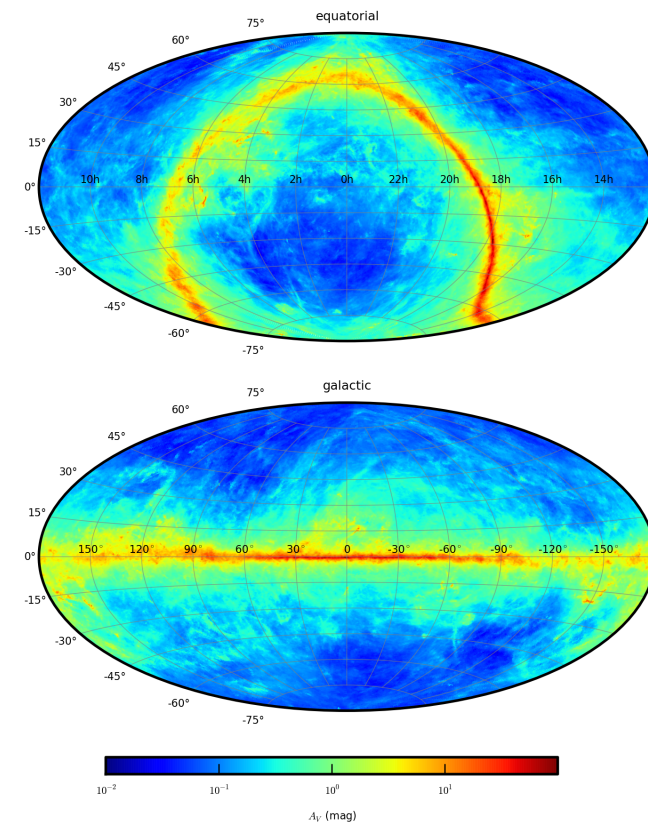
Figura 16: Representation of the map of extinction obtained by the Planck mission.
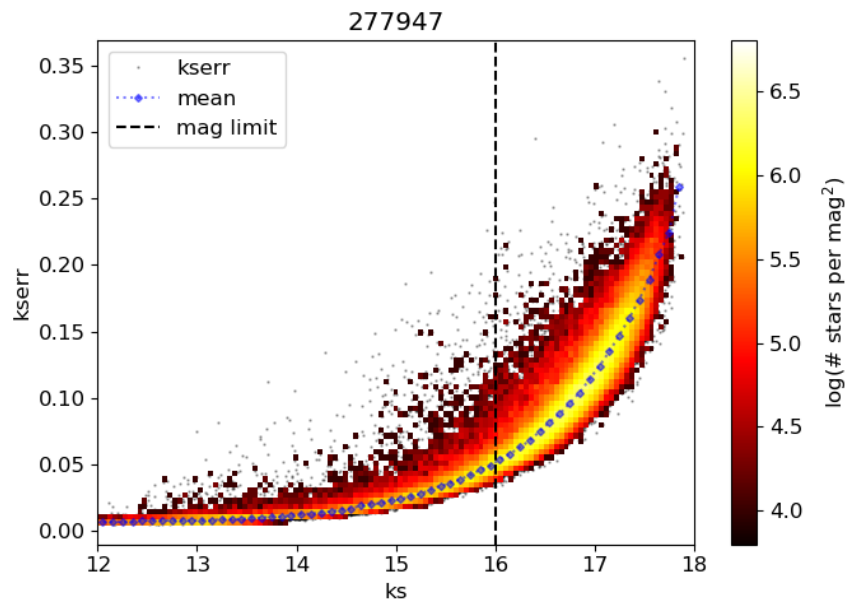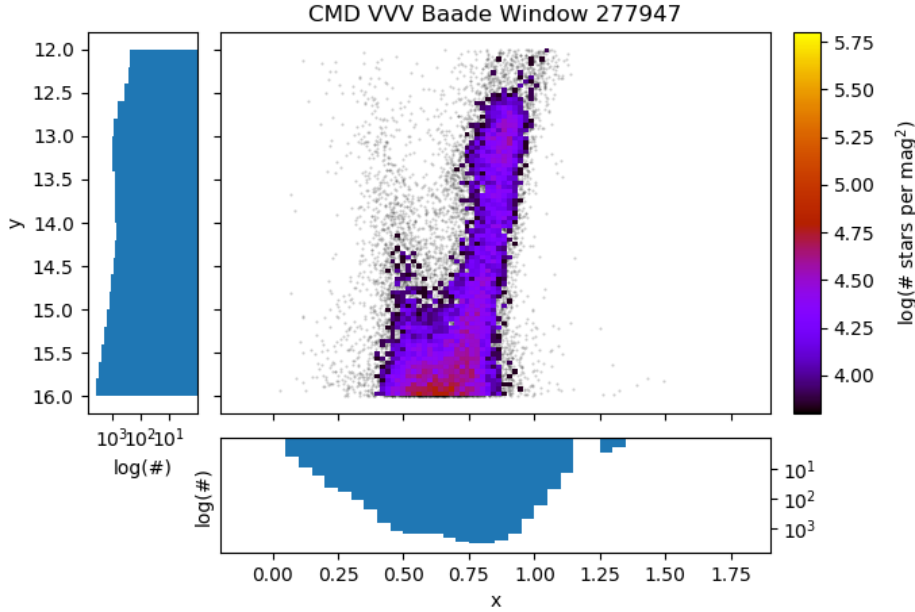

Figura 17: Distribution of photometric errors in Baade's Window. The colour refers to density of stars in an area of width 0.05 mag and height 0.004 mag. The vertical black dashed line marks the magnitude limit that was used for the fitting procedure. The blue diamonds and the underlying blue dotted line show the mean value given as input to TRILEGAL.

Figura 18: Central panel: observed colour-magnitude diagram of Baade Window; the colour represents the density of stars per square magnitude in boxes with a side of 0.05 mag along the magnitude axis and 0.02 mag along the colour one. Left panel: luminosity function in logarithmic scale. Bottom panel: colour function in logarithmic scale.

3.3 BAADE WINDOW

Baade's Window is a region of the Milky Way located at $(l, b) = (1.0317°, -3.9097°)$ characterised by a very low value of extinction ($A_V \sim 1.6$ mag). Differently from the majority of the lines of sight, it allows observations to reach the typical distances of the Bulge and even further and clearly offers a unique chance to study in detail this complex component of the Galaxy. As such, it is suitable for testing the output of TRILEGAL against the observations.

The observed colour-magnitude diagram of Baade Window obtained from the VVV source catalogue is showed in Figure 18: both the Disk component and the Bulge component are present. The comparison with the colour-magnitude diagram constructed from the output of the TRILEGAL model apparently did not highlight any serious mismatch.

Nevertheless, a deeper analysis focused on the luminosity function actually showed a small discrepancy between the simulations and the observations. In
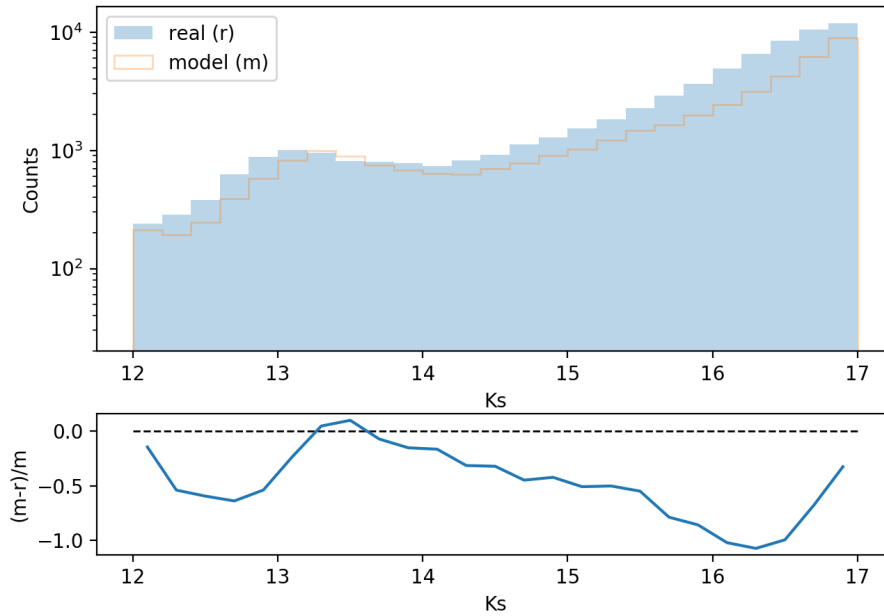
Figura 19: Upper panel: comparison between the observed and the simulated luminosity function in Baade Window. The blue, filled histogram shows the LF obtained from the VVV source catalogue; the light brown, empty histogram shows the simulated LF. Lower panel: residual trend.

fact, as shown in Figure 19, the simulated LF appeared fainter than the observed one and the shift amounted to about 0.2 mag. The cause of this deviation is unclear and most likely was caused by the improvement of the libraries of models that TRILEGAL uses to simulate the Galaxy. It is also possible that the high quality of the data (high resolution and faint magnitude limit) played a role in underlining this mismatch.

Either way, this evidence implied that some of the parameters of the model had to be revised to provide a better result. From the observed shift of the LF, the expected new value of $R_\odot$ could be quickly estimated and resulted in an expected decrease of about 9% of the value used in the simulation, corresponding to a relocation from $R_\odot = 8700\text{pc}$ to about $R_\odot \sim 7900\text{pc}$. This estimate, as will be illustrated in the next chapter, was not so far from the result of the revision.

4 | RECALIBRATION

In the previous section the mismatch between output of TRILEGAL and the VVV data was presented, hinting at the need to recalibrate the model. Since a complete revision of its whole, large set of parameters cannot be performed easily and requires suitable numerical techniques, a preliminary recalibration focused on the Bulge component alone is presented in the following sections, providing new values for two key parameters of the code: the bulge central density ρ_{bulge} and the distance from the Sun to the Galactic Centre $R_\odot$.

4.1 MINIMIZATION ALGORITHM

To determine the values of the parameters that provide the best fit of the output of the model to the VVV catalogue a non-linear numerical method that iteratively seeks the minimum of a function of the residuals (cost function) is required. The Levenberg-Marquardt method was selected since it is often implemented in this kind of problems for its ability to solve non-linear least squares problems using a trust-region approach and an approximation of the cost function, as described below.

4.1.1 Levenberg–Marquardt algorithm

Let us consider the estimated vector of parameters at iteration i, θ_i, and a region of radius h_i centred on it called trust region. The updated vector of parameters θ_{i+1} is initially determined by means of a Gauss-Newton step, which involves the determination of a descent direction and of a length α_i that has be covered to reach the minimum on that specific direction. Before applying this update to the current estimate of the parameters, the length α_i is compared with the current size of the trust-region: if it falls inside the trust region it is accepted as is and the algorithm proceeds normally; in the opposite case, a new update $\bar{\alpha}_i$ is computed such that it falls inside the trust region, following a direction close to the deepest descent. In the latter case, the size of the trust region is also adjusted according to the goodness of the approximation of the cost function.

All these operations were performed by the function `least_squares` from

the NumPy package[1] of the Python programming language. It uses a cost function in the form

$$F(x) = \frac{1}{2} \sum_{0}^{m-1} \left(l(r_i(x)^2) \right)$$

(13)

where $r(x)$ are the residuals (in general an m-dimensional real function of n real variables) and l is the loss function used to reduce the effect of outliers, which in the default case does nothing and simply returns the residuals with no transformation applied. It should be noted that the cost function is equivalent to a χ^2 in this case.

The default parameters of the function were used, with the exception of the relative step size for the finite difference approximation of the Jacobian that was set to 5% to avoid numerical issues. In fact, using the "optimum" relative step determined automatically by the function itself produced a variation of the cost function so small that the whole procedure would suffer from an early interruption and would just return the starting parameters.

4.1.2 Fitting the luminosity function

The initial setup involved an approximation of the selected fields by their closest Healpix at the desired resolution; the values of A_V and σ_{A_V} were then retrieved from the corresponding pixels on the Planck map (Planck Collaboration et al., 2014). The limiting magnitude was set to $K_s = 18$ mag for all of the simulations given the magnitude limit of the VVV survey and the VISTA photometric system was selected in the input file.

At this point the minimization started: the `least_squares` function was called once per field specifying some initial estimates of ρ_{bulge} and $R_\odot$ and a Python function that returned the residuals $\Delta N = N_{sim} - N_{VVV}$. In detail, this function ran the simulation with the given parameters and returned the residuals between the simulated and the real luminosity function, both binned in a magnitude interval $[m_{min}, m_{max}]$ with a step m_{step}. The Levenberg-Marquardt algorithm evaluated the cost function using different combinations of parameter values and converged to the new parameter set that was finally returned and written to file.

---

[1] http://www.numpy.org/
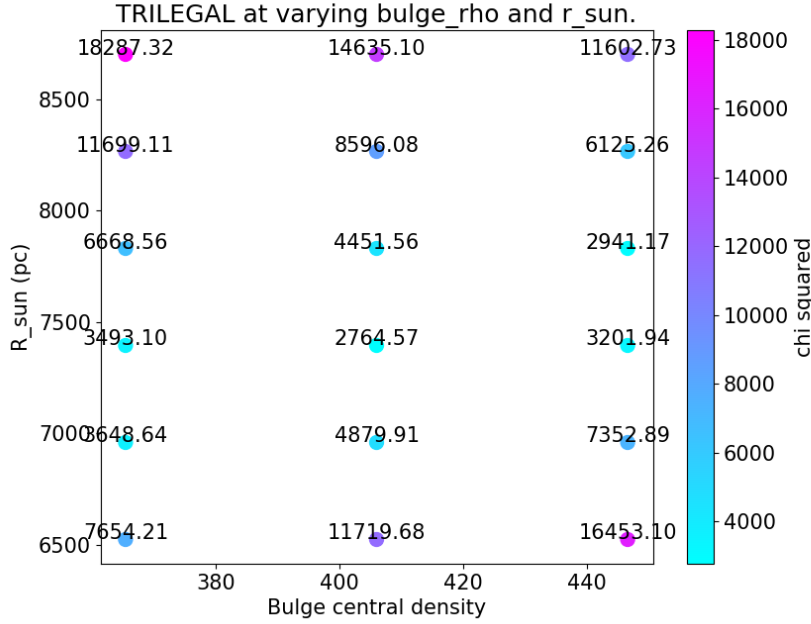
Figura 20: Initial evaluation of models on a simple grid. Each point corresponds to a pair of ρ_{bulge} and $R_{\odot}$ and the colour represents the χ^2 of the model. Over each point the exact value of the χ^2 is indicated.

4.2 BEST PARAMETERS DETERMINATION ON BW

The calibration procedure was firstly applied to the luminosity function from Baade Window (BW) or, to be more precise, from the Healpix pixel of $N_{side} = 256$ number 277947, which contains the central position of the window and is characterised by $A_V = 1.63$ mag.

4.2.1 Preparatory analysis

Prior to applying the automatic algorithm on BW, the parameters space was subject to an exploratory analysis. A grid of parameter values was investigated using $\rho_{bulge} = [365.4, 406.0, 446.6] \, M_{\odot}/pc^3$ and $R_{\odot} = [6525.0, 6960.0, 7395.0, 7830.0, 8265.0, 8700.0]$ pc and the χ^2 (equivalent to the cost function as explained above) was computed at each grid point; the result can be seen in Figure 20. It was evident that there was some degeneration between the parameters: based only on the values of the χ^2 a low value of $R_{\odot}$ and ρ_{bulge}, such as $R_{\odot} = 6960.0$ pc and $\rho_{bulge} = 356.4 \, M_{\odot}/pc^3$, could produce a fit as good as the one that would

be obtained with a high value of both, for example $R_\odot = 7395.0$ pc and $\rho_{\text{bulge}} = 446.6\ \text{M}_\odot/\text{pc}^3$.

4.2.2 Early recalibration

The first attempt at automatically recalibrating TRILEGAL on this field was performed taking into account all the stars with magnitude from $K_s = 12$ mag to $K_s = 18$ mag and binning the luminosity function using a step of 0.2 mag; its result was partly successful. While the minimization proceeded smoothly and without issues, the simulated luminosity function looked different from the real one, possibly because the algorithm was influenced by the large residuals in the high magnitude region of the luminosity function.

Several corrections had to be applied to the minimization procedure to reach a reasonable result; they are explained in the following.

4.2.3 Photometric errors

It is important to notice that, as mentioned in the previous chapter, TRILEGAL does not include by default any error on the photometry and produces "perfect" magnitudes, that is without errors. The comparison with VVV presented above was then incomplete and was probably one of the reasons why the resulting fit was poor. From this moment onwards, the photometric errors were included in TRILEGAL as explained in the section 3.2.

4.2.4 Luminosity function magnitude cut

In the previous chapter, Figure 17 illustrated the mean errors at different magnitudes provided to TRILEGAL as blue diamonds; they became bigger than the bin width of the luminosity function (0.2 mag) at magnitudes larger than about $K_s = 17.5$ mag. This meant that the LF had to be limited at this or lower magnitudes, but it was not evident where to cut it.

To investigate the effects arising from a cut of the luminosity function at a magnitude m_{lim} three grids of χ^2, were computed from the same simulation output using different limiting magnitudes. The cuts were made at $K_s = 17$, 16 and 15 mag and the resulting grids are presented in Figure 21. Each plot shows that an absolute minimum likely existed at a larger bulge central density and a lower Sun-GC distance with respect to the original values, though the exact location seemed different for each limiting magnitude. In the case with $m_{\text{lim}} = 16$ mag the position of the minimum appeared to be located at very large densities, possibly larger than the maximum value of the grid and differently from the other two that suggested instead less drastic values.
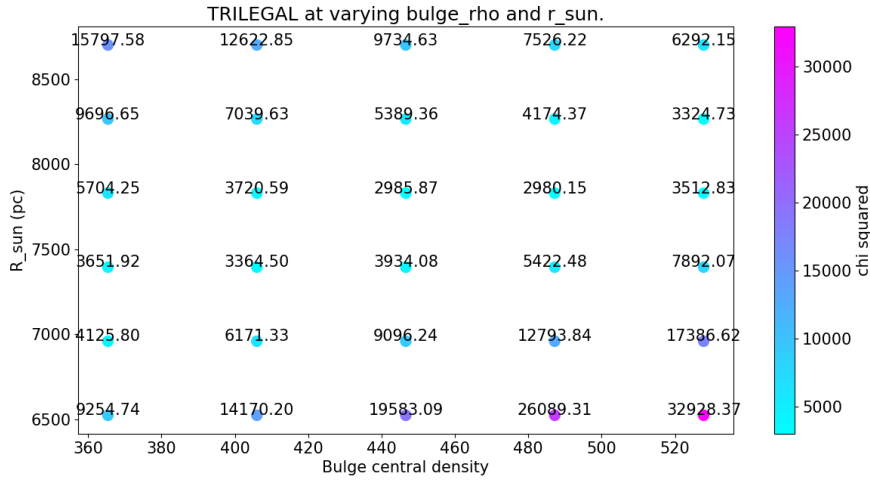
(a) Magnitude limit set at $K_S = 17$ mag.
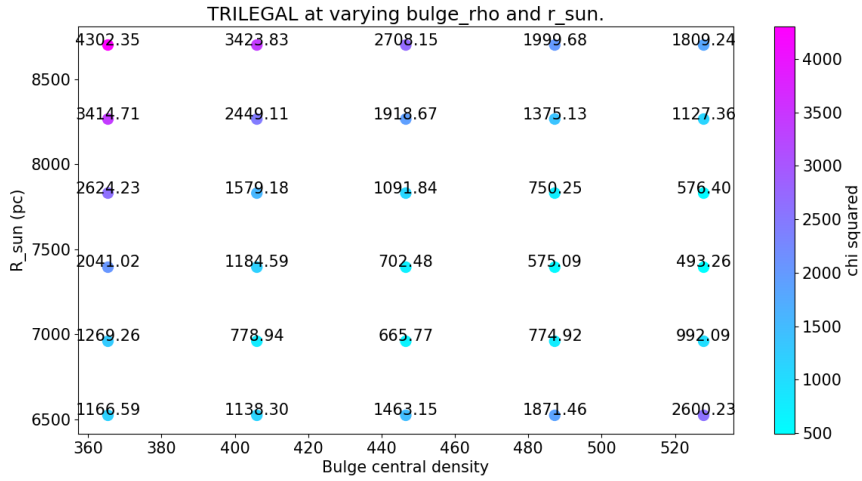
(b) Magnitude limit set at $K_S = 16$ mag.
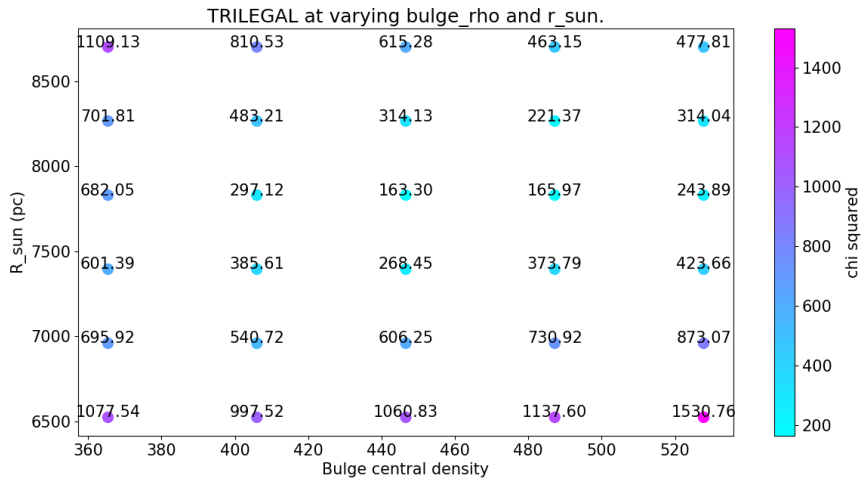
(c) Magnitude limit set at $K_S = 15$ mag.

Figura 21: Grids of χ^2 of the models using different magnitude cuts on the LF.

Figura 22: LF from a TRILEGAL simulation with $\rho_{\mathrm{bulge}} = 527.8\ \mathrm{M}_\odot/\mathrm{pc}^3$ and $R_\odot = 7395.0$ pc.

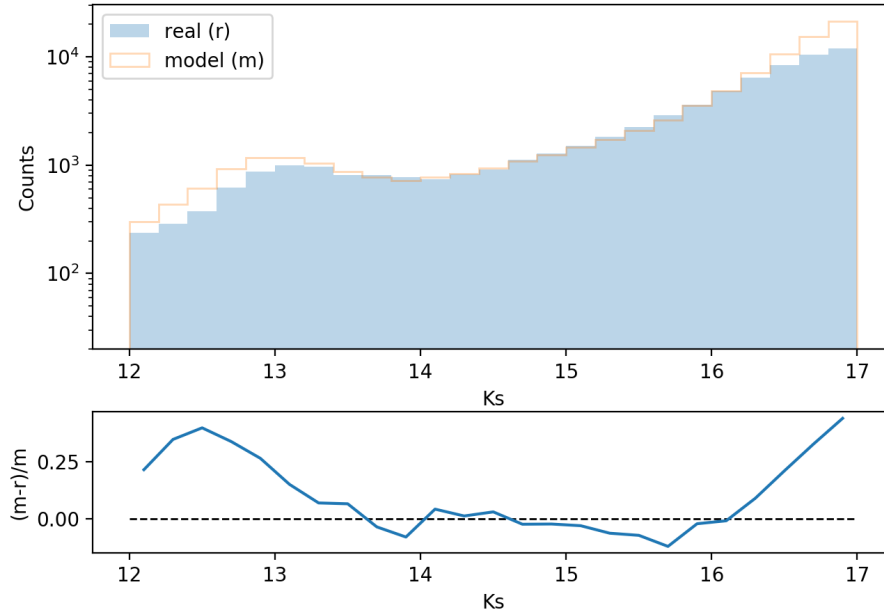Figure 22 illustrates the luminosity function in the case $m_{\mathrm{lim}} = 17$ and shows the possible reason for this behaviour. At magnitudes larger than 16 mag the observed and simulated luminosity functions differ significantly and the χ^2 will be large unless the fit minimizes the residuals over the whole magnitude interval, balancing the need to fit simultaneously the RC and the high magnitude region. Using $m_{\mathrm{lim}} = 15$ mag on the other hand would remove the numerous fainter stars, allowing the RC to be properly weighted and consequently better fitted. In the intermediate case of $m_{\mathrm{lim}} = 16$ mag the mismatch at large magnitudes is absent thus the χ^2 will be the lower the better the fit is for the magnitude range between 15 mag and 16 mag because it contains a large number of stars and then predominantly influences its value.

Anyway, $m_{\mathrm{lim}} = 15$ mag was discarded due to the low number of stars that were present in the resultant magnitude range, while the $m_{\mathrm{lim}} = 17$ mag case was discarded due to being too close to the region with error ~ 0.2 mag. The limiting magnitude for the subsequent analysis was then set to $m_{\mathrm{lim}} = 16$ mag. The final result was satisfactory and likely to have weak dependence on the specific magnitude cut.

4.2.5 Zero point correction

Another detail to be taken into consideration is that the photometric system used by VISTA did not match exactly the standard Vega system which instead is used in TRILEGAL. This meant that small corrections had to be applied to the photometry of the VVV stars before they could be used as a reference for the simulations. These corrections were derived using the equations

$$
\begin{aligned}
Z_{\text{VISTA}} - J_{\text{2MASS}} &= 1.025(J-H)_{\text{2MASS}} + 0.082 \\
Y_{\text{VISTA}} - J_{\text{2MASS}} &= 0.610(J-H)_{\text{2MASS}} + 0.074 \\
J_{\text{VISTA}} - J_{\text{2MASS}} &= -0.077(J-H)_{\text{2MASS}} + 0.026 \\
H_{\text{VISTA}} - H_{\text{2MASS}} &= 0.032(J-H)_{\text{2MASS}} - 0.017 \\
K_{s\text{VISTA}} - K_{s\text{2MASS}} &= 0.010(J-K_s)_{\text{2MASS}} + 0.003
\end{aligned}
\tag{14}
$$

from appendix B of Rubele et al. (2015). For the J and K_s bands in particular these equations resulted in an offset of 0.026 mag and 0.003 mag respectively between the model Vega-magnitudes and the CASU calibrations (Rubele et al., 2015):

$$
\begin{aligned}
J - J_{VISTA} &= 0.026 \\
K_{\mathbf{s}} - K_{\text{s},VISTA} &= 0.003
\end{aligned}
\tag{15}
$$

where J and K_s are in the Vegamag photometric system while J_{VISTA} and $K_{\text{s},VISTA}$ are in the VISTA one. It is clear that these adjustments amounted to a small fraction of the original values, thus they had a minimal effect on the results of the fit and were included for the sake of completeness.

4.2.6 Poissonian χ^2

Looking for the best fit minimizing the standard χ^2 actually assumes that the data under study follows a Gaussian distribution. In case this requirement is not satisfied the resulting fit won't be really correct. Since the data used in this section is more appropriately described by a Poisson distribution, the equivalent of the χ^2 illustrated in Dolphin (2002) is used:

$$
-2\ln PLR = 2\sum_i m_i - n_i + n_i \ln \frac{n_i}{m_i}
\tag{16}
$$

where PLR stands for Poisson Likelihood Ratio, n_i is the observed value at bin i, m_i is the model value at bin i.
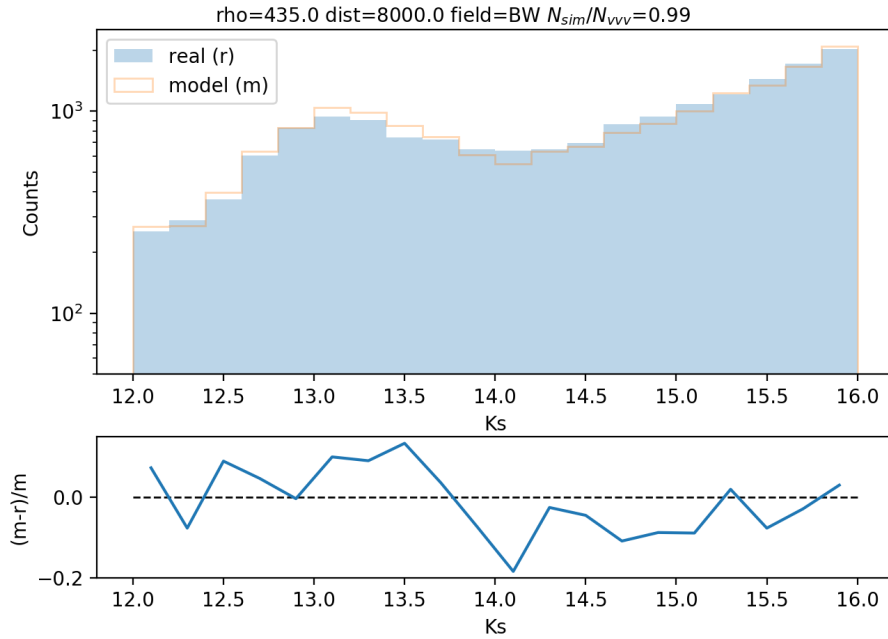
Figura 23: Upper panel: luminosity function of the best model for Baade Window. Lower panel: residuals between the simulated and the observed luminosity function.

4.2.7 Colour cut

One last, fundamental decision had a bigger impact on the goodness of the fit: most of the disk stars were excluded through a colour cut independent on luminosity. To give an example and clarify the previous statement, this meant that for Baade Window the colour magnitude diagram in Figure 18 was vertically cut off at a colour $C_{cut} = 0.60$ mag and only stars with a colour larger than this value were retained. As a result of this choice, the minimization process took into account mostly stars from the Bulge, indeed producing better fits.

The determination of the position of the colour cut in this work was performed manually on each field but, in future applications, it will be calculated relying on more accurate methods to provide a better star selection. However, in the future thorough recalibration of TRILEGAL the disk stars will have to be included to constrain also the disk parameters.

Label	l (deg)	b (deg)	$A^a_{V,Sumi}$ (mag)	$A^b_{V,Planck}$ (mag)	$A^b_{V,Green2015}$ (mag)
2	2.33	-3.46	1.51	1.71	1.97
7	-0.14	-5.91	1.34	1.38	-
13	7.91	-3.58	2.05	2.29	2.09
14	5.23	2.81	2.49	2.64	3.13
17	5.28	-3.45	1.92	2.41	2.86
25	-2.32	-3.56	2.33	2.86	-
27	-4.92	-3.65	1.69	2.11	-
29	-6.64	-4.62	1.53	2.01	-
40	-2.99	-3.14	2.92	3.10	-

[a]Sumi (2004); [b]Planck Collaboration et al. (2014); [c]Green et al. (2015)

Tabella 2: List of the fields used in the present work. The labels correspond to the identifiers of the fields in the OGLE survey.

4.2.8 Final result

Putting all of the previous corrections together, the best fit parameters for BW turned out to be $\rho_{bulge} = 435.0$ M$_\odot$/pc^3 and $R_\odot = 8000.0$ pc. The comparison between the simulated and observed LFs is shown in Fig. 23. The position of the RC was clearly well reproduced by the simulation, but the number of stars resulted a little bit too large. On the other hand, the tail of the LF was well fitted. In particular, this figure shows that the problem caused by the tail of the LF mentioned above was still present, though widely mitigated.

4.3 VERIFICATION ON OGLE FIELDS

To determine whether the best fit parameters obtained on BW were adequate, several low-extinction fields were used as a test; they are listed in Table 2. Notably, these were a subset of the fields from the OGLE survey and were also used in the paper by Vanhollebeke, Groenewegen, and Girardi (2009), though the fields number 8 and 47 were excluded since they are located outside of the region of the Bulge covered by VVV.

This examination revealed how differently some fields behaved with the parameters derived on BW. Figures 24(a) and 24(b) illustrate two good cases: the LF is reproduced fairly well in both the number of stars and the position

of the RC; the field number 27 specifically shows some issues at the head of the distribution. Figure 24(c) shows a good match of the number of stars but a wrong position of the RC; Figure 24(d) presents the opposite case, a good reproduction of the position but not of the number of stars. Finally, Figure 24(e) shows an LF for which the match is not good.

4.3.1 Refitting OGLE fields

Looking for the Bulge density and the Sun-GC distance on Baade Window alone and expecting these values to be suitable for any other field was definitely a too ambitious demand as is obvious from the previous discussion. Moreover, using only two parameters was clearly limiting the chances of obtaining a globally good recalibration.

A better assessment of the recalibration could be obtained determining the best fit parameters on each field listed in Table 2. In addition to providing a more reliable parameter determination, this approach could be used to determine if the shape of the bulge implemented in the model was appropriate. In fact, in this case the fields closest or farthest from the centre would have showed a relatively bad fit.

Each field was subject to the same automatic minimization procedure applied to Baade Window to determine the best fit parameters. The picture that emerged was coherent with what was illustrated in the panels of Figure 24. Some fields were fitted with parameters similar to those determined on BW while others showed much different values. For instance, in the case of field number 27 the parameters resulted $\rho_{\text{bulge}} = 450 \ M_{\odot}/\text{pc}^3$, similar to the one for BW, and $R_{\odot} = 8295$ pc, similar to the BW one but probably influenced by the discrepancy at the head of the LF. On the other hand, for field number 13 the final parameters were $\rho_{\text{bulge}} = 385 \ M_{\odot}/\text{pc}^3$ and $R_{\odot} = 8015$ pc, not as different from the ones for BW as Figure 24(e) would suggest.

4.4 TOWARDS A GLOBAL RECALIBRATION

The results obtained from fitting each field separately provided a multifaceted and not conclusive view of the bulge. Ideally, the best choice at this point would have been to fit all the fields at the same time so that the minimization procedure would seek the global minimum with the strictest constraint available. Regrettably, the algorithm would easily fall into local minima, that in this case would be much more numerous than in the fit of a single one.
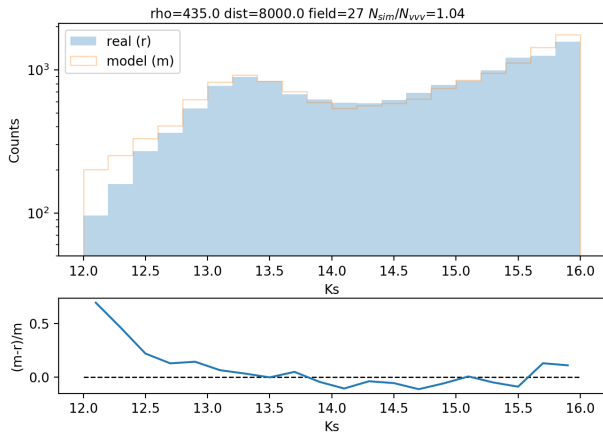
(a) Field 27, good fit with BW parameters.
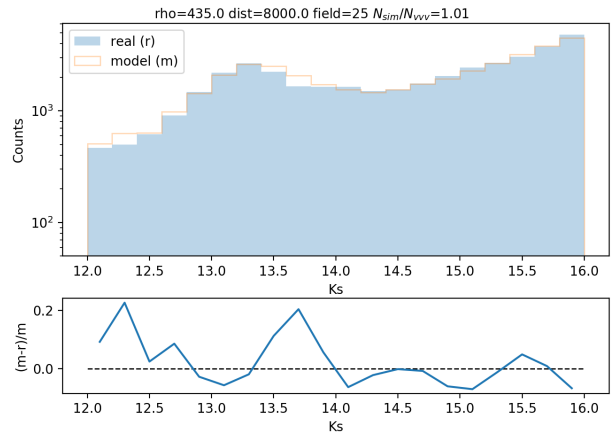
(b) Field 25; good fit with BW parameters.
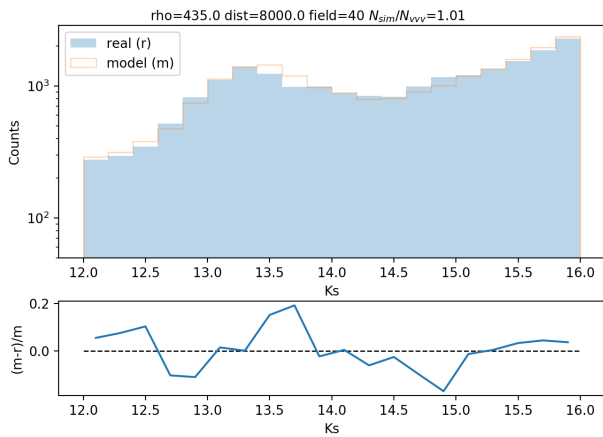
(c) Field 40, position of RC is shifted but number of stars would be reproduced fairly well.
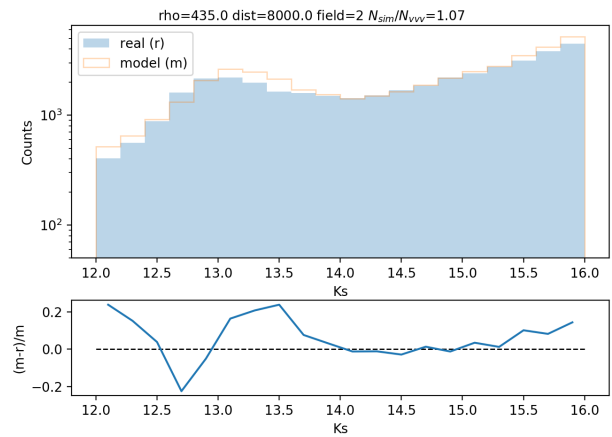
(d) Field 2, the position is correct but the number of stars is not well reproduced.
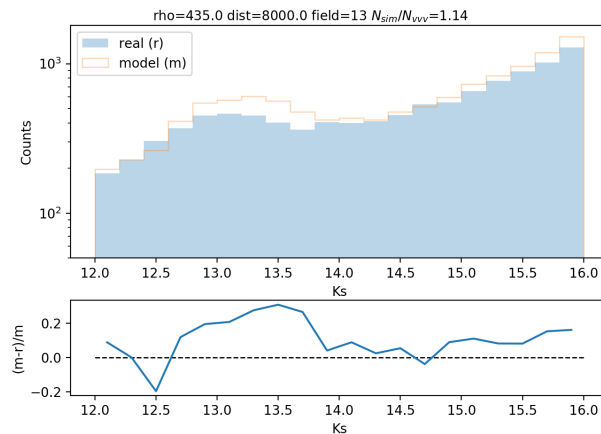
(e) Field 13, both the position and the number of stars are not reproduced.

Figura 24: Result of using the best fit parameters obtained on Baade Window to simulate other fields scattered over the region of the Bulge.

4.4.1 χ^2 grid

With these notions in mind, a simpler albeit less accurate procedure to determine the best fit parameters can be adopted. Instead of iteratively minimizing the residuals between the simulations and the observations, the χ^2 was evaluated on a grid of (ρ_{bulge}, $R_\odot$) for each field. Subsequently, the grids for all of the fields were superimposed, in the sense that they were summed grid-point wise, and an approximation of the global minimum was recovered.

The outcome of the previous methods could still be used as a starting point in the determination of the size of the grid and its spacing. Considering ρ_{bulge}, its best values varied from about 370 $M_\odot/\text{pc}^3$ to about 525 $M_\odot/\text{pc}^3$ but the grid was extended to cover the larger interval $\rho_{\text{bulge}} \in [300, 750]$ $M_\odot/\text{pc}^3$ using an initial step of $\Delta\rho_{\text{bulge}} = 50$ $M_\odot/\text{pc}^3$. Similarly, the best values of $R_\odot$ ranged in between 7685 pc and 8750 pc but the grid was extended to $R_\odot \in [7000, 8750]$ pc with an initial spacing of $\Delta R_\odot = 250$ pc. In total, there were 80 grid points and therefore 80 χ^2 values for each field. The grids for some of the fields that were used for Figure 24 are shown in Figure 25. It is possible to appreciate that different combination of parameters can produce similarly good results.

4.4.2 New best parameters

The final grid, obtained summing the single grids of each field, is illustrated in Figure 26. Summing the grids had a very large impact on the best model identification: even if for each single field the best value could hardly be identified, in the cumulative grid the region that contained the best parameters set was much clearer.

Grid-wise, the absolute minimum was found for $\rho_{\text{bulge}} = 400$ $M_\odot/\text{pc}^3$ and $R_\odot = 7750$ pc. These values were reasonable: the parameter related to the central density of the bulge almost resulted equal to its original value while the other parameter changed dramatically from its starting value but resulted consistent with the estimates found in the literature.

4.4.3 Global χ^2 map

To better visualize this result a last set of simulations was performed implementing the best fit values presented above. Afterwards, the values of the χ^2 obtained on each field were plotted on a map in galactic coordinate at the position of their respective fields. This map is illustrated in Figure 27. Overall the result seems quite good but some remarks are needed.

The field with the worst fit is number 14, at $l = 5.23°$ ad $b = 2.81°$. This is in part caused by an abrupt decrease in the number of stars found in the

(a) Reduced χ^2 grid for the field number 2.

(b) Reduced χ^2 grid for the field number 27.

(c) Reduced χ^2 grid for the field number 13.

(d) Reduced χ^2 grid for the field number 25.
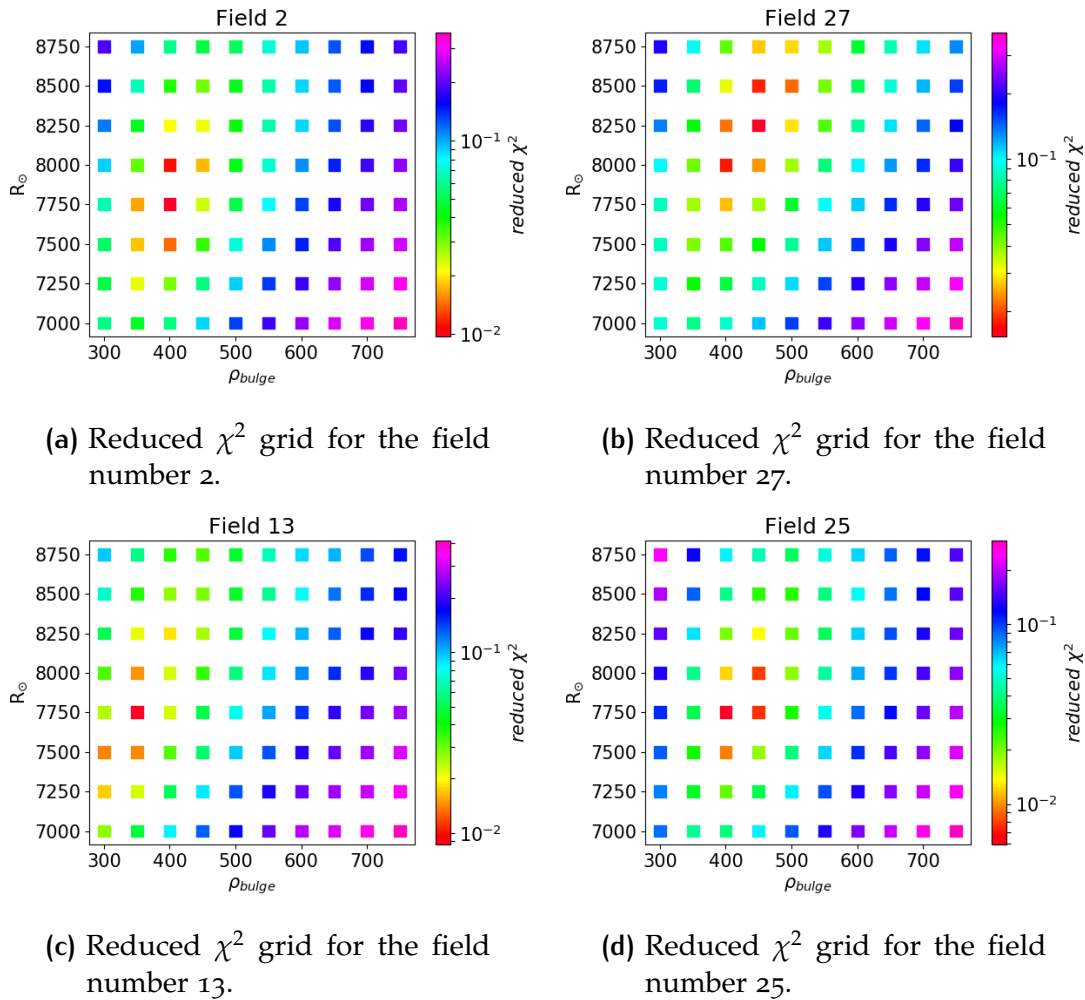
Figura 25: Examples of the reduced χ^2 grid obtained on some fields.

luminosity function of pixel 289693 below 12.4 mag. Also, this field is the only one located at a positive Galactic latitude and this fact may concur in producing a bad result. Finally, another cause may be found in the relatively high absorption associated with this region and it is in fact the third largest one of the fields considered in this work.

The second field that needs attention is the number 7, located at $l = -0.14°$ $b = -5.91°$. The reason why a bad fit is obtained is not clear. A deeper investigation will be carried out in the future.

Finally, the gradient of χ^2 along galactic longitude needs to be highlighted. This fact likely points towards the need to include another parameter in the discussion, the scale length of the bulge. More generally, it is possible that the

Figura 26: Grid of the summed χ^2 obtained summing the values from each individual field on the grid points.

Figura 27: Location of the fields in Galactic coordinates; the color stands for the value of the χ^2.
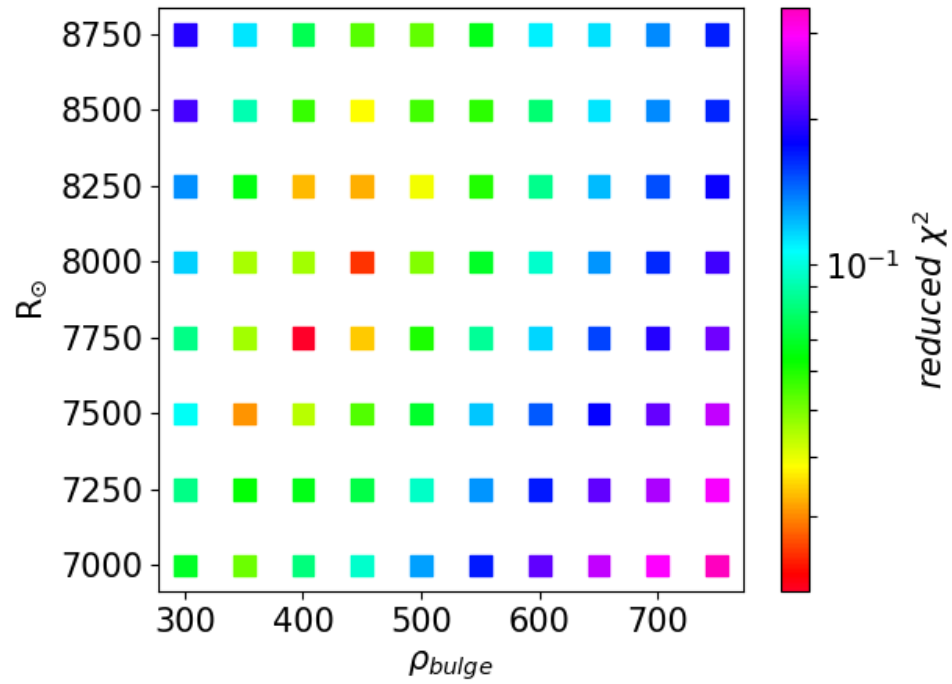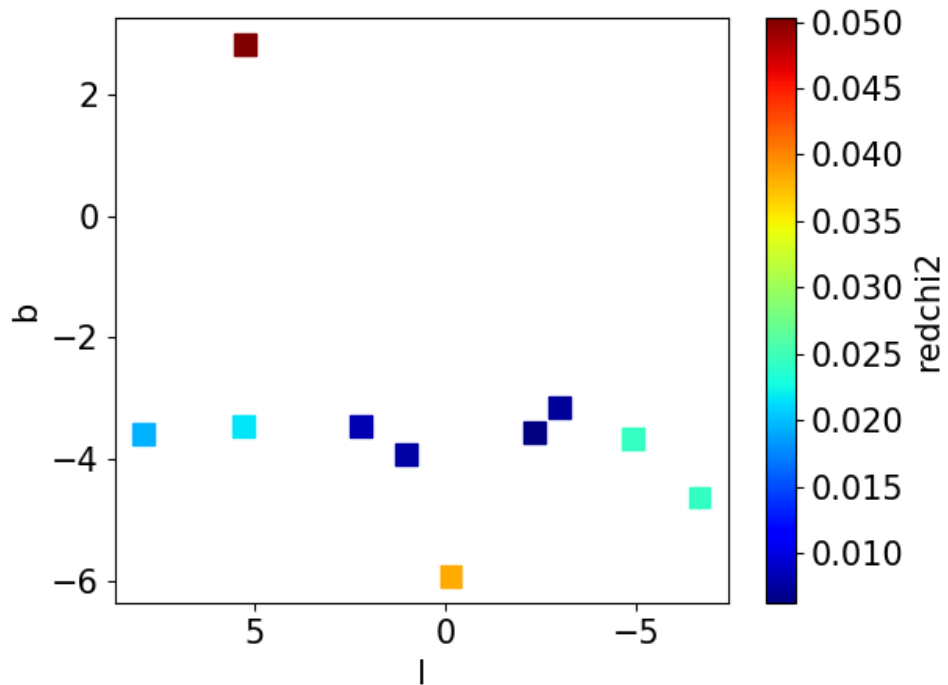
shape of the bulge as currently implemented in TRILEGAL, based on the work by Vanhollebeke et al. using 2MASS data, may not be suitable to explain the deep catalogue produced from the VVV survey. This will be investigated in a future work.

4.4.4 Error estimation

Considering Figure 26 it is evident that the position of the maximum is tied to the grid. This results in an uncertainty on the parameters of the best model that, given the spacing of the grid itself, amounts to $\Delta\rho_{\text{bulge}} = 25\ \text{M}_\odot/\text{pc}^3$ and $\Delta R_\odot = 125$ pc. These arguably represent a naive and loose estimate of the errors.

Actually, due to the methods implemented in this work to determine the best model, deriving an estimate of the true errors on the best fit parameters is complicated.

On the other hand it is quite easy to estimate the statistical errors associated with this result: it is sufficient to run a large enough number of simulations and study the resulting χ^2 distribution, whose dispersion can then be turned into a confidence region around the best fit model. It was decided to run 100 simulations of the best model with the same parameters and Figure 28 presents the resulting distribution of χ^2. Fitting a gaussian function to this distribution yields a mean chi-square of 4428.0 and a sigma of 131.0, but the specific values are dependent on the bin size, though weakly. Figure 29 illustrates the confidence region, defined as the region of points whose χ^2 differs from the best model of up to 3σ, superimposed on a grid similar to that in Figure 26 with the only difference of not using the reduced χ^2. To construct this region first of all the χ^2 grid was interpolated with using the `Rbf` interpolator provided in the `scipy`[2] module, then the contour corresponding to 3σ over the minimum value of the χ^2 was computed and marked in the figure in cyan.

The statistical errors alone, producing such a small confidence region, give a rough idea of the goodness of the data used in this work but do not provide a complete picture of the uncertainties. In fact, systematic errors could be hidden in the model as an incomplete representation of shape the bulge. This issue will be properly investigated when the recalibration will be extended to take into account a larger number of fields spread on the whole bulge and by taking into account parameters that were not investigated in this work such as the 3D distribution of the dust.
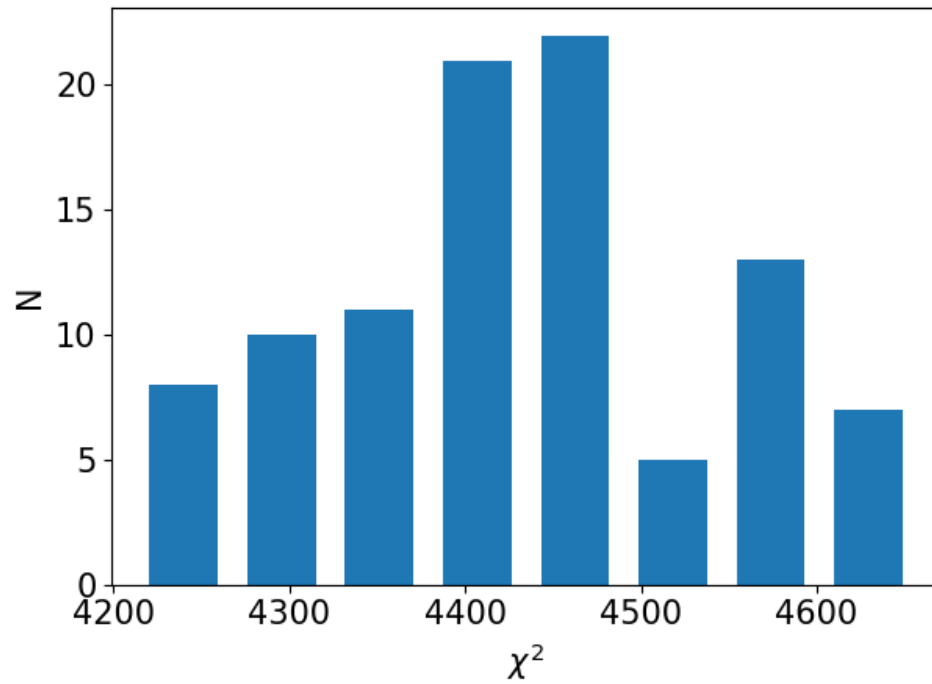
---

[2] https://scipy.org/

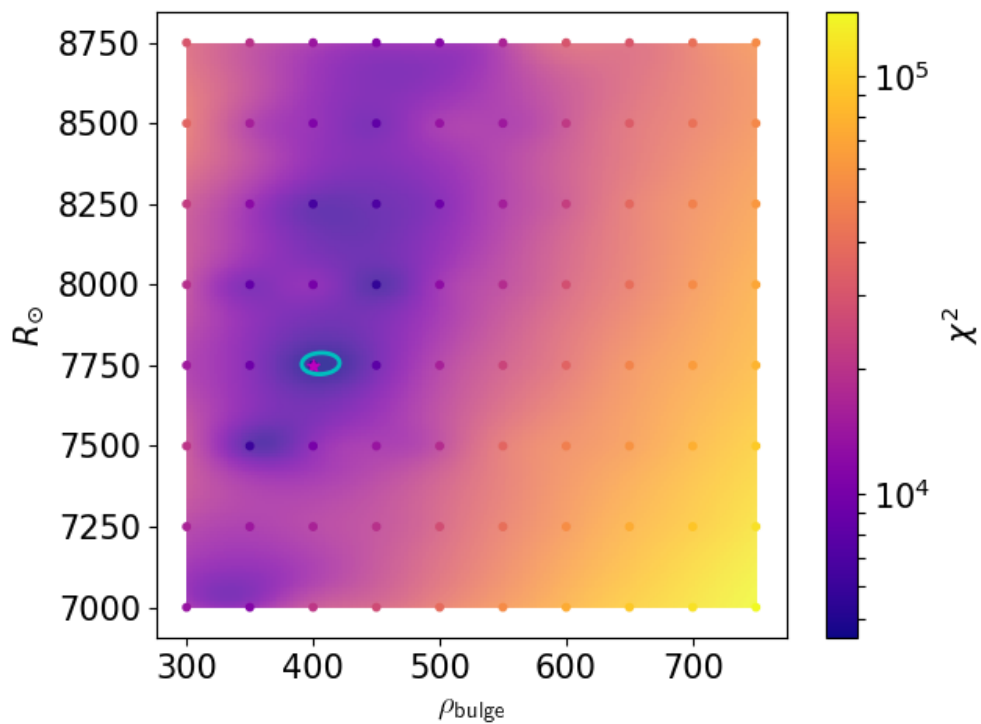**Figura 28:** Distribution of χ^2 obtained from running 100 simulations of the best model.

Figura 29: Grid of χ^2 equivalent to the one presented in Figure 26. A 2D fit produced with the `scipy` module of the Python language is added and the 3σ region around the best model, marked with a magenta coloured star, is shown in cyan.

5 | CONCLUSION

The population synthesis code TRILEGAL can simulate the photometry of any field in the MW accounting for the SFH, the AMR, the IMF, the different components of the MW and the photometric system. The Vista Variables in the Via Lactea is a high quality infrared photometric survey that covers more than 300 squared degrees on the Galactic Centre, including the bulge region and its neighbourhood. The comparison of the luminosity functions of Baade Window constructed from a simulation with TRILEGAL and from the VVV data highlighted a slight mismatch (Figure 19), whose cause has not yet been identified but may be related to the refinement of the models at the base of the code.

Anyway, a revision of the parameters used in TRILEGAL was needed to recover a proper reproduction of the luminosity distribution of the stars. This work focused on the bulge region and specifically took care of determining new values for the bulge central density ρ_{bulge} and for the Sun-Galactic Centre distance $R_\odot$.

Initially, only Baade Window was subject to a detailed analysis. The existence of a minimum was investigated computing a sparse grid of χ^2 (Figure 20) that indeed pointed to the existence of a region where the minimum was likely located. A Levenberg-Marquardt algorithm was implemented to pinpoint with higher accuracy the values of the parameters at the minimum of the χ^2, but the result was not completely satisfactory. In fact the simulated luminosity function still did not closely reproduce the observed one (Figure 22).

To overcome this issue a number of adjustments were considered. First of all the magnitude range of the LF was restricted to $K_s \in [12, 16]$ mag to prevent the large photometric errors found in the tail from influencing too much the fit and to avoid the saturation of the brightest stars. Then, a zero point correction (Equation 14), though fairly small, was applied to VVV to bring it from the VISTA photometric system to the standard Vegamag one used by TRILEGAL. Also, a Poisson equivalent of the χ^2 was implemented. Finally, a colour cut for each field was introduced on both the observed and the simulated stars to remove most of the disk stars and concentrate on fitting the Bulge ones.

These procedures indeed allowed the minimization to proceed without problems and to determine a new set of parameters, namely $\rho_{\text{bulge}} = 435.0 \, \text{M}_\odot/\text{pc}^3$

and $R_\odot$ = 8000 pc. However, when these were applied to the fields listed in Table 2 the fit looked non-homogeneous. Some fields were fitted correctly while others would have required a different set of parameters. Actually, it was unreasonable to expect that from BW alone a perfect fit for the whole bulge region could be achieved just by adjusting two of the many parameters of the model.

Applying the minimization procedure on each field individually provided evidence to support the previous statement. The derived parameters were spread in a range of bulge densities and Sun-GC distances, making the determination of a global recalibration hard to achieve though the minimization. An ideal solution would have been to fit together all the fields at the same time to attain the overall best fit, but this process was subject to falling into local minima much more easily than the one applied to a single field.

The best choice was then to explore the parameters space of the fields computing a grid of χ^2 for each field and later summing them all together to check for the existence of a minimum. The grid consisted of 80 grid points for $\rho_{\text{bulge}} \in [300, 750]$ M$_\odot$/pc^3 with a step of 50 M$_\odot$/pc^3 and $R_\odot \in [7000, 8750]$ pc with a spacing of 250 pc. This approach showed that the global minimum definitely existed and was located around (ρ_{bulge}, $R_\odot$)=(400 M$_\odot$/pc^3, 7750 pc) (Figure 26). These values will be used as the starting point for the subsequent more accurate recalibration of the code.

Due to the methods used in the derivation of the best model, the determination of the uncertainty on the parameter values wads complicated. The statistical errors on the other hand could be easily estimated. A large number of simulations (100) of the best model were performed and from each the χ^2 value was calculated. The resulting χ^2 distribution was then used to mark a 3σ region of statistical error (Figure 29).

5.1 FUTURE PROSPECTS AND IMPROVEMENTS

The work presented here provided an initial recalibration of two key parameters of the TRILEGAL code. Even if a deep analysis was not carried out, this result can be used as the starting point for a more detailed process of recalibration of the code that will take into account a larger set of parameters. This will obviously require more time and sophisticated numerical techniques to take into account the difficulty of the task. Specifically, a few points that have to be improved in this work need to be pointed out.

NUMBER OF FIELDS A larger number of fields distributed as homogeneously as possible over the largest possible area of the bulge region must be considered to provide the most comprehensive determination of the set of parameters. In fact, this work considered fields which were located mostly around $b = -4°$, with only one field in the Northern region of the Bulge: the result could be slightly biased and cannot discern whether the vertical scale height of the bulge is appropriate or not.

DEVIANT FIELDS The result for the only field at positive galactic latitude is relatively bad compared to the others, but under no means this should be taken as proof that asymmetries are present in the structure of the Bulge, which would require more accurate analysis.

Likewise, albeit less strongly, also the field located at $b \approx -6°$ is badly fitted but in this case the reason is not yet clear.

Both these anomalies may be resolved by increasing the coverage of the Bulge and/or by fitting other parameters of the code.

EXTINCTION The extinction map used in this work is the Planck one and the specific values in the V band for each field are listed in the fifth column of Table 2; this however is not the only choice. The fourth column presents extinction values used in the paper by Vanhollebeke et al. (2009) and taken from Sumi (2004) while the sixth column lists the values from Green et al. (2015), which unfortunately did non not cover all of the fields. A more recent choice is also offered by Green et al. (2018). Given the different values of absorption found in these three maps, the result of the fit may change significantly from one map to the other.

Actually, the 3D map by Green et al. (2015) or the updated one by Green et al. (2018) will be tested in future simulations to determine if an improvement of the fit can be achieved.

ERROR ESTIMATE A more complete estimate of the errors has be established to assess the goodness of the parameters determination. In fact, the approach used in this work only derived the statistical errors associated with the result and cannot be considered exhaustive.

CALIBRATION OF EVOLUTIONARY MODELS FOR THE TP-AGB PHASE The thermally pulsing AGB (TP-AGB) is one of the most uncertain evolutionary phases of single stars. By fitting the luminosity functions and the colour-magnitude diagrams of the brighter stars (~ 3 mag above the red clump) across the bulge, we have the possibility of testing, and ultimately calibrating, the evolutionary

models for this phase at the low stellar masses ($M \sim 1$ M$_\odot$) and moderately high metallicities that characterize the bulge population.

This work would however require: 1) examining a very large area across the bulge, in order to have large numbers of TP-AGB stars; 2) having already derived the correct morphology and distribution of the dust for the Bulge. Therefore, after the above-mentioned recalibration of bulge parameters, we will proceed with the recalibration of the TP-AGB models included in TRILEGAL.

BIBLIOGRAFIA

J. Alonso-García, M. Mateo, B. Sen, M. Banerjee, M. Catelan, D. Minniti, and K. von Braun. Uncloaking Globular Clusters in the Inner Galaxy. *AJ*, 143:70, Mar. 2012. doi: 10.1088/0004-6256/143/3/70.

J. Alonso-García, R. K. Saito, M. Hempel, D. Minniti, J. Pullen, M. Catelan, R. Contreras Ramos, N. J. G. Cross, O. A. Gonzalez, P. W. Lucas, T. Palma, E. Valenti, and M. Zoccali. Milky Way demographics with the VVV survey. IV. PSF photometry from almost one billion stars in the Galactic bulge and adjacent southern disk. *ArXiv e-prints*, art. arXiv:1808.06139, Aug. 2018.

T. Bensby, S. Feltzing, and M. S. Oey. Exploring the Milky Way stellar disk. A detailed elemental abundance study of 714 F and G dwarf stars in the solar neighbourhood. *A&A*, 562:A71, Feb. 2014. doi: 10.1051/0004-6361/201322631.

J. Binney, O. Gerhard, and D. Spergel. The photometric structure of the inner Galaxy. *MNRAS*, 288:365–374, June 1997. doi: 10.1093/mnras/288.2.365.

J. Bland-Hawthorn and O. Gerhard. The Galaxy in Context: Structural, Kinematic, and Integrated Properties. *Annual Review of Astronomy and Astrophysics*, 54:529–596, Sept. 2016. doi: 10.1146/annurev-astro-081915-023441.

J. A. Cardelli, G. C. Clayton, and J. S. Mathis. The Relationship between Infrared, Optical, and Ultraviolet Extinction. *ApJ*, 345:245, Oct. 1989. doi: 10.1086/167900.

G. Chabrier. The Galactic Disk Mass Budget. I. Stellar Mass Function and Density. *ApJ*, 554:1274–1281, June 2001. doi: 10.1086/321401.

G. de Vaucouleurs. General Physical Properties of External Galaxies. *Handbuch der Physik*, 53:311, Jan. 1959.

I. Dékány, D. Minniti, M. Catelan, M. Zoccali, R. K. Saito, M. Hempel, and O. A. Gonzalez. VVV Survey Near-infrared Photometry of Known Bulge RR Lyrae Stars: The Distance to the Galactic Center and Absence of a Barred Distribution of the Metal-poor Population. *ApJ*, 776:L19, Oct. 2013. doi: 10.1088/2041-8205/776/2/L19.

A. E. Dolphin. Numerical methods of star formation history measurement and applications to seven dwarf spheroidals. *MNRAS*, 332:91–108, May 2002. doi: 10.1046/j.1365-8711.2002.05271.x.

E. Dwek, R. G. Arendt, M. G. Hauser, T. Kelsall, C. M. Lisse, S. H. Moseley, R. F. Silverberg, T. J. Sodroski, and J. L. Weiland. Morphology, Near-Infrared Luminosity, and Mass of the Galactic Bulge from COBE DIRBE Observations. *ApJ*, 445:716, June 1995. doi: 10.1086/175734.

O. J. Eggen, D. Lynden-Bell, and A. R. Sandage. Evidence from the motions of old stars that the Galaxy collapsed. *ApJ*, 136:748, Nov. 1962. doi: 10.1086/147433.

L. Girardi, G. Bertelli, A. Bressan, C. Chiosi, M. A. T. Groenewegen, P. Marigo, B. Salasnich, and A. Weiss. Theoretical isochrones in several photometric systems. I. Johnson- Cousins-Glass, HST/WFPC2, HST/NICMOS, Washington, and ESO Imaging Survey filter sets. *A&A*, 391:195–212, Aug. 2002. doi: 10.1051/0004-6361:20020612.

L. Girardi, M. A. T. Groenewegen, E. Hatziminaoglou, and L. da Costa. Star counts in the galaxy. stimulating from very deep to very shallow photometric surveys with the trilegal code. *A&A*, 436:895–915, June 2005. doi: 10.1051/0004-6361:20042352.

L. Girardi, J. Dalcanton, B. Williams, R. de Jong, C. Gallart, M. Monelli, M. A. T. Groenewegen, J. A. Holtzman, K. A. G. Olsen, A. C. Seth, D. R. Weisz, and the ANGST/ANGRRR Collaboration. Revised Bolometric Corrections and Interstellar Extinction Coefficients for the ACS and WFPC2 Photometric Systems. *Publications of the Astronomical Society of the Pacific*, 120:583, May 2008. doi: 10.1086/588526.

O. A. Gonzalez, M. Rejkuba, D. Minniti, M. Zoccali, E. Valenti, and R. K. Saito. The inner Galactic bar traced by the VVV survey. *A&A*, 534:L14, Oct. 2011. doi: 10.1051/0004-6361/201117959.

K. M. Górski, E. Hivon, A. J. Banday, B. D. Wandelt, F. K. Hansen, M. Reinecke, and M. Bartelmann. HEALPix: A Framework for High-Resolution Discretization and Fast Analysis of Data Distributed on the Sphere. *ApJ*, 622:759–771, Apr. 2005. doi: 10.1086/427976.

G. M. Green, E. F. Schlafly, D. P. Finkbeiner, H.-W. Rix, N. Martin, W. Burgett, P. W. Draper, H. Flewelling, K. Hodapp, N. Kaiser, R. P. Kudritzki, E. Magnier,

N. Metcalfe, P. Price, J. Tonry, and R. Wainscoat. A Three-dimensional Map of Milky Way Dust. *ApJ*, 810:25, Sept. 2015. doi: 10.1088/0004-637X/810/1/25.

G. M. Green, E. F. Schlafly, D. Finkbeiner, H.-W. Rix, N. Martin, W. Burgett, P. W. Draper, H. Flewelling, K. Hodapp, N. Kaiser, R.-P. Kudritzki, E. A. Magnier, N. Metcalfe, J. L. Tonry, R. Wainscoat, and C. Waters. Galactic reddening in 3D from stellar photometry - an improved map. *MNRAS*, 478:651–666, July 2018. doi: 10.1093/mnras/sty1008.

Y.-W. Lee and S. Jang. Common Origin of Two RR Lyrae Populations and the Double Red Clump in the Milky Way Bulge. *ApJ*, 833:236, Dec. 2016. doi: 10.3847/1538-4357/833/2/236.

Y.-W. Lee, S.-J. Joo, and C. Chung. The Milky Way without X: an alternative interpretation of the double red clump in the Galactic bulge. *MNRAS*, 453: 3906–3911, Nov. 2015. doi: 10.1093/mnras/stv1980.

M. López-Corredoira. A case against an X-shaped structure in the Milky Way young bulge. *A&A*, 593:A66, Sept. 2016. doi: 10.1051/0004-6361/201527074.

M. López-Corredoira. Absence of an X-shaped Structure in the Milky Way Bulge Using Mira Variable Stars. *ApJ*, 836:218, Feb. 2017. doi: 10.3847/1538-4357/836/2/218.

D. Minniti, P. W. Lucas, J. P. Emerson, R. K. Saito, M. Hempel, P. Pietrukowicz, A. V. Ahumada, M. V. Alonso, J. Alonso-Garcia, J. I. Arias, R. M. Bandyopad-hyay, R. H. Barbá, B. Barbuy, L. R. Bedin, E. Bica, J. Borissova, L. Bronfman, G. Carraro, M. Catelan, J. J. Clariá, N. Cross, R. de Grijs, I. Dékány, J. E. Drew, C. Fariña, C. Feinstein, E. Fernández Lajús, R. C. Gamen, D. Geisler, W. Gieren, B. Goldman, O. A. Gonzalez, G. Gunthardt, S. Gurovich, N. C. Hambly, M. J. Irwin, V. D. Ivanov, A. Jordán, E. Kerins, K. Kinemuchi, R. Kurtev, M. López-Corredoira, T. Maccarone, N. Masetti, D. Merlo, M. Messineo, I. F. Mirabel, L. Monaco, L. Morelli, N. Padilla, T. Palma, M. C. Parisi, G. Pignata, M. Rejkuba, A. Roman-Lopes, S. E. Sale, M. R. Schreiber, A. C. Schröder, M. Smith, J. , L. Sodré, M. Soto, M. Tamura, C. Tappert, M. A. Thompson, I. Toledo, M. Zoccali, and G. Pietrzynski. VISTA Variables in the Via Lactea (VVV): The public ESO near-IR variability survey of the Milky Way. *New A*, 15:433–443, July 2010. doi: 10.1016/j.newast.2009.12.002.

M. Ness and D. Lang. The X-shaped Bulge of the Milky Way Revealed by WISE. *AJ*, 152:14, July 2016. doi: 10.3847/0004-6256/152/1/14.

Planck Collaboration, A. Abergel, P. A. R. Ade, N. Aghanim, M. I. R. Alves,
G. Aniano, C. Armitage-Caplan, M. Arnaud, M. Ashdown, F. Atrio-Barandela,
J. Aumont, C. Baccigalupi, A. J. Banday, R. B. Barreiro, J. G. Bartlett, E. Bat-
taner, K. Benabed, A. Benoît, A. Benoit-Lévy, J. P. Bernard, M. Bersanelli,
P. Bielewicz, J. Bobin, J. J. Bock, A. Bonaldi, J. R. Bond, J. Borrill, F. R. Bouchet,
F. Boulanger, M. Bridges, M. Bucher, C. Burigana, R. C. Butler, J. F. Cardoso,
A. Catalano, A. Chamballu, R. R. Chary, H. C. Chiang, L. Y. Chiang, P. R.
Christensen, S. Church, M. Clemens, D. L. Clements, S. Colombi, L. P. L.
Colombo, C. Combet, F. Couchot, A. Coulais, B. P. Crill, A. Curto, F. Cuttaia,
L. Danese, R. D. Davies, R. J. Davis, P. de Bernardis, A. de Rosa, G. de Zotti,
J. Delabrouille, J. M. Delouis, F. X. Désert, C. Dickinson, J. M. Diego, H. Dole,
S. Donzelli, O. Doré, M. Douspis, B. T. Draine, X. Dupac, G. Efstathiou, T. A.
Enßlin, H. K. Eriksen, E. Falgarone, F. Finelli, O. Forni, M. Frailis, A. A.
Fraisse, E. Franceschi, S. Galeotta, K. Ganga, T. Ghosh, M. Giard, G. Giardino,
Y. Giraud-Héraud, J. González-Nuevo, K. M. Górski, S. Gratton, A. Gregorio,
I. A. Grenier, A. Gruppuso, V. Guillet, F. K. Hansen, D. Hanson, D. L. Harrison,
G. Helou, S. Henrot-Versillé, C. Hernández- Monteagudo, D. Herranz, S. R.
Hildebrandt, E. Hivon, M. Hobson, W. A. Holmes, A. Hornstrup, W. Hovest,
K. M. Huffenberger, A. H. Jaffe, T. R. Jaffe, J. Jewell, G. Joncas, W. C. Jones,
M. Juvela, E. Keihänen, R. Keskitalo, T. S. Kisner, J. Knoche, L. Knox, M. Kunz,
H. Kurki-Suonio, G. Lagache, A. Lähteenmäki, J. M. Lamarre, A. Lasenby,
R. J. Laureijs, C. R. Lawrence, R. Leonardi, J. León-Tavares, J. Lesgourgues,
F. Levrier, M. Liguori, P. B. Lilje, M. Linden-Vørnle, M. López-Caniego, P. M.
Lubin, J. F. Macías-Pérez, B. Maffei, D. Maino, N. Mandolesi, M. Maris,
D. J. Marshall, P. G. Martin, E. Martínez-González, S. Masi, M. Massardi,
S. Matarrese, F. Matthai, P. Mazzotta, P. McGehee, A. Melchiorri, L. Mendes,
A. Mennella, M. Migliaccio, S. Mitra, M. A. Miville-Deschênes, A. Moneti,
L. Montier, G. Morgante, D. Mortlock, D. Munshi, J. A. Murphy, P. Naselsky,
F. Nati, P. Natoli, C. B. Netterfield, H. U. Nørgaard-Nielsen, F. Noviello, D. No-
vikov, I. Novikov, S. Osborne, C. A. Oxborrow, F. Paci, L. Pagano, F. Pajot,
R. Paladini, D. Paoletti, F. Pasian, G. Patanchon, O. Perdereau, L. Perotto,
F. Perrotta, F. Piacentini, M. Piat, E. Pierpaoli, D. Pietrobon, S. Plaszczyn-
ski, E. Pointecouteau, G. Polenta, N. Ponthieu, L. Popa, T. Poutanen, G. W.
Pratt, G. Prézeau, S. Prunet, J. L. Puget, J. P. Rachen, W. T. Reach, R. Rebolo,
M. Reinecke, M. Remazeilles, C. Renault, S. Ricciardi, T. Riller, I. Ristorcelli,
G. Rocha, C. Rosset, G. Roudier, M. Rowan- Robinson, J. A. Rubiño-Martín,
B. Rusholme, M. Sandri, D. Santos, G. Savini, D. Scott, M. D. Seiffert, E. P. S.
Shellard, L. D. Spencer, J. L. Starck, V. Stolyarov, R. Stompor, R. Sudiwala,
R. Sunyaev, F. Sureau, D. Sutton, A. S. Suur-Uski, J. F. Sygnet, J. A. Tauber,

D. Tavagnacco, L. Terenzi, L. Toffolatti, M. Tomasi, M. Tristram, M. Tucci, J. Tuovinen, M. Türler, G. Umana, L. Valenziano, J. Valiviita, B. Van Tent, L. Verstraete, P. Vielva, F. Villa, N. Vittorio, L. A. Wade, B. D. Wandelt, N. Welikala, N. Ysard, D. Yvon, A. Zacchei, and A. Zonca. Planck 2013 results. XI. All-sky model of thermal dust emission. *A&A*, 571:A11, Nov. 2014. doi: 10.1051/0004-6361/201323195.

S. Rubele, L. Girardi, L. Kerber, M.-R. L. Cioni, A. E. Piatti, S. Zaggia, K. Bekki, A. Bressan, G. Clementini, R. de Grijs, J. P. Emerson, M. A. T. Groenewegen, V. D. Ivanov, M. Marconi, P. Marigo, M.-I. Moretti, V. Ripepi, S. Subramanian, B. L. Tatton, and J. T. van Loon. The VMC survey - XIV. First results on the look-back time star formation rate tomography of the Small Magellanic Cloud. *MNRAS*, 449:639–661, May 2015. doi: 10.1093/mnras/stv141.

R. K. Saito, M. Hempel, D. Minniti, P. W. Lucas, M. Rejkuba, I. Toledo, O. A. Gonzalez, J. Alonso-García, M. J. Irwin, E. Gonzalez- Solares, S. T. Hodgkin, J. R. Lewis, N. Cross, V. D. Ivanov, E. Kerins, J. P. Emerson, M. Soto, E. B. Amôres, S. Gurovich, I. Dékány, R. Angeloni, J. C. Beamin, M. Catelan, N. Padilla, M. Zoccali, P. Pietrukowicz, C. Moni Bidin, F. Mauro, D. Geisler, S. L. Folkes, S. E. Sale, J. Borissova, R. Kurtev, A. V. Ahumada, M. V. Alonso, A. Adamson, J. I. Arias, R. M. Bandyopadhyay, R. H. Barbá, B. Barbuy, G. L. Baume, L. R. Bedin, A. Bellini, R. Benjamin, E. Bica, C. Bonatto, L. Bronfman, G. Carraro, A. N. Chenè, J. J. Clariá, J. R. A. Clarke, C. Contreras, A. Corvillón, R. de Grijs, B. Dias, J. E. Drew, C. Fariña, C. Feinstein, E. Fernández-Lajús, R. C. Gamen, W. Gieren, B. Goldman, C. González-Fernández, R. J. J. Grand, G. Gunthardt, N. C. Hambly, M. M. Hanson, K. G. Hełminiak, M. G. Hoare, L. Huckvale, A. Jordán, K. Kinemuchi, A. Longmore, M. López-Corredoira, T. Maccarone, D. Majaess, E. L. Martín, N. Masetti, R. E. Mennickent, I. F. Mirabel, L. Monaco, L. Morelli, V. Motta, T. Palma, M. C. Parisi, Q. Parker, F. Peñaloza, G. Pietrzyński, G. Pignata, B. Popescu, M. A. Read, A. Rojas, A. Roman-Lopes, M. T. Ruiz, I. Saviane, M. R. Schreiber, A. C. Schröder, S. Sharma, M. D. Smith, L. Sodré, J. Stead, A. W. Stephens, M. Tamura, C. Tappert, M. A. Thompson, E. Valenti, L. Vanzi, N. A. Walton, W. Weidmann, and A. Zijlstra. VVV DR1: The first data release of the Milky Way bulge and southern plane from the near-infrared ESO public survey VISTA variables in the Vía Láctea. *A&A*, 537:A107, Jan. 2012. doi: 10.1051/0004-6361/201118407.

P. L. Schechter, M. Mateo, and A. Saha. DoPHOT, A CCD Photometry Program: Description and Tests. *Publications of the Astronomical Society of the Pacific*, 105: 1342, Nov. 1993. doi: 10.1086/133316.

T. Sumi. Extinction map of the Galactic centre: OGLE-II Galactic bulge fields. *MNRAS*, 349:193–204, Mar. 2004. doi: 10.1111/j.1365-2966.2004.07482.x.

E. Vanhollebeke, M. A. T. Groenewegen, and L. Girardi. Stellar populations in the Galactic bulge. Modelling the Galactic bulge with TRILEGAL. *A&A*, 498: 95–107, Apr. 2009. doi: 10.1051/0004-6361/20078472.

C. Wegg and O. Gerhard. Mapping the three-dimensional density of the Galactic bulge with VVV red clump stars. *MNRAS*, 435:1874–1887, Nov. 2013. doi: 10.1093/mnras/stt1376.